The 2020 M_w 6.5 Monte Cristo Range, Nevada, Earthquake: Anatomy of a Crossing-Fault Rupture through a Region of Highly Distributed Deformation

Israporn Sethanant*[1], Edwin Nissen[1], Léa Pousse-Beltran[2], Eric Bergman[3], and Ian Pierce[4]

ABSTRACT

The 15 May 2020 M_w 6.5 Monte Cristo Range earthquake (MCRE) in Nevada, United States, is the largest instrumental event in the Mina deflection—a zone of east-trending left-lateral faults accommodating a right step between northwest-trending right-lateral faults of the Walker Lane. The MCRE ruptured a highly distributed faulting area with muted geomorphic expressions, motivating us to characterize the behavior of an earthquake on a structurally immature fault system. Inverse modeling of Interferometric Synthetic Aperture Radar (InSAR) and Global Navigation Satellite System (GNSS) displacements reveals left-lateral slip on an east-striking, eastern fault and left-lateral–normal slip on an east-northeast-striking, western fault. Unusually, the two faults cross one another and ruptured together in the mainshock. The maximum slip of 1 m occurs at 8–10 km depth, but less than 0.1 m of slip reaches the surficial model fault patches, yielding a pronounced shallow slip deficit (SSD) of 91%. Relocated hypocenters indicate that the mainshock initiated at 9 km depth and that aftershocks span depths of 1–11 km, constraining the local seismogenic thickness. Our new field observations of fracturing and pebble-clearing in the western MCRE characterize a third, shorter, northern fault that is at the resolution limit of the InSAR–GNSS modeling. The segmented and intersecting fault geometry, off-fault aftershocks with variable mechanisms, distributed surface fractures, limited long-term geomorphic offsets, and a 600–700 m (cumulative) bedrock offset are all characteristic of a structurally immature fault system. However, the large SSD is not unusual for an earthquake of this magnitude, and a larger compilation of InSAR models (28 $M_w \geq$ 6.4 strike-slip events) shows that SSDs correlate with magnitude rather than structural maturity. This study demonstrates the importance of integrating geodesy, seismology, and field observations to capture the full complexity of large earthquakes, and further suggests that seismic hazard assessments in shattered crustal regions consider the potential for multi- and cross-fault rupture.

KEY POINTS

- The Monte Cristo Range mainshock ruptured obliquely crossing faults.
- Discrepancies between geodesy, seismology, and geology illuminate unusual fault zone complexity.
- Magnitude has a stronger influence on shallow slip deficit than maturity, affecting seismic hazard assessment.

Supplemental Material

INTRODUCTION

Fault segmentation is known to play an important role in earthquake rupture propagation and arrest. The influential "characteristic earthquake" model posits that the maximum earthquake magnitudes are limited by the lengths of discrete, mapped fault segments and their intervening segment

---

1. School of Earth and Ocean Sciences, University of Victoria, British Columbia, Canada, https://orcid.org/0000-0003-0962-8999 (IS); 2. Université Grenoble Alpes, Université Savoie Mont Blanc, CNRS, IRD, Université Gustave Eiffel, ISTerre, Grenoble, France, https://orcid.org/0000-0003-2833-411X (LP-B); 3. Global Seismological Services, Golden, Colorado, U.S.A., https://orcid.org/0000-0002-7069-8286 (EB); 4. Department of Earth Sciences, University of Oxford, Oxford, United Kingdom, https://orcid.org/0000-0002-1865-2512 (IP)

*Corresponding author: isethanant@uvic.ca

Cite this article as Sethanant, I., E. Nissen, L. Pousse-Beltran, E. Bergman, and I. Pierce (2023). The 2020 M_w 6.5 Monte Cristo Range, Nevada, Earthquake: Anatomy of a Crossing-Fault Rupture through a Region of Highly Distributed Deformation, *Bull. Seismol. Soc. Am.* **113**, 948–975, doi: 10.1785/0120220166

boundaries (Schwartz and Coppersmith, 1984; Wesnousky, 2006). However, in the recent years this simple view has been complicated by observations of a number of multifault earthquakes that have jumped across major segment boundaries to achieve larger rupture areas and magnitudes than would normally be anticipated (e.g., Hicks and Rietbrock, 2015; Huang *et al.*, 2016; Nissen *et al.*, 2016; Hamling *et al.*, 2017). Fault segmentation is one manifestation of fault structural maturity—a term that describes the evolution of fault zone properties with incremental offset. In this progression, a fault core thickens (e.g., Robertson, 1983; Scholz, 1987; Hull, 1988; Childs *et al.*, 2009), off-fault damage intensifies (e.g., Shipton and Cowie, 2001; Finzi *et al.*, 2009; Faulkner *et al.*, 2011; Savage and Brodsky, 2011; Aben *et al.*, 2016), and the fault trace simplifies as segments coalesce and asperities are smoothed out (e.g., Walsh and Watterson, 1988; Wesnousky, 1988; Peacock and Sanderson, 1991; Childs *et al.*, 1995; Stirling *et al.*, 1996; Frost *et al.*, 2009; Wechsler *et al.*, 2010; Brodsky *et al.*, 2011). Structural maturity may also be important in controlling other aspects of earthquake rupture behavior. Observations suggest that earthquakes along structurally mature faults exhibit more localized deformation and narrower aftershock distributions (Powers and Jordan, 2010; Zinke *et al.*, 2015; Hatem *et al.*, 2017; Perrin *et al.*, 2021), faster rupture velocities (Perrin *et al.*, 2016; Chounet *et al.*, 2018), more persistent rupture directivity (Kane *et al.*, 2013; Aderhold and Abercrombie, 2015), proportionally more surface slip (Dolan and Haravitch, 2014), larger amounts of aseismic afterslip (Johanson *et al.*, 2006; Feng *et al.*, 2010; Thomas *et al.*, 2014; Li *et al.*, 2020), smaller overall stress drops and weaker near-field ground motions (Choy and Kirby, 2004; Manighetti *et al.*, 2007; Radiguet *et al.*, 2009; Hecker *et al.*, 2010), and lower rates of dynamic aftershock triggering (Gomberg, 1996) than those along immature faults. Mature faults may also exhibit steadier interseismic strain accumulation (Wang *et al.*, 2021) and more regular recurrence intervals (Berryman *et al.*, 2012; Thakur and Huang, 2021).

These relationships illustrate how the structural setting of an earthquake, including fault segmentation and structural maturity, could have an important bearing on seismic hazard, for example, by influencing potential rupture lengths and magnitudes, amounts and distributions of slip, and involvement of multiple faults. They raise the possibility of incorporating easily observed metrics for structural maturity, such as fault cumulative offset, age, slip rate, length, and surface trace complexity (Choy and Kirby, 2004; Manighetti *et al.*, 2007, 2021), in hazard assessments and earthquake early warning algorithms (Dolan and Haravitch, 2014; Perrin *et al.*, 2016; Hutchison *et al.*, 2020). However, other factors including fault geometry and kinematic style, tectonic environment, and rheology of ruptured material may also influence earthquake behavior, potentially complicating matters (e.g., Oskin *et al.*, 2012; Teran *et al.*, 2015). To clarify these relations further, careful observations are needed of earthquakes from a range of structural and geological settings, and which span the full spectrum of fault structural maturity.

The M_w 6.5 Monte Cristo Range earthquake (MCRE) ruptured on 15 May 2020 at 11:03 UTC (4:03 a.m. local time) mostly along previously unmapped faults in the Mina deflection zone within the central Walker Lane, Nevada (Wesnousky, 2005; Fig. 1). The evolution of the Mina deflection since the Miocene has given rise to a region of conspicuously varied lithology and geometrically complex faulting (Wetterauer, 1977; Oldow *et al.*, 1994, 2008). Fault segments mapped in the western Mina deflection, just west of the MCRE, are relatively short (on average 1–3 km with a maximum segment length of ~10 km), highly distributed, and variably oriented (Dohrenwend, 1982; Oldow *et al.*, 1994), and some of them reactivate inherited structures (Wetterauer, 1977; Oldow *et al.*, 2008). Faults and fault-bounded blocks within the Mina deflection are thought to rotate about vertical axes to accommodate dextral shear transfer across the Walker Lane (Wesnousky, 2005). This crustal rotation potentially diverts the faults away from being favorable to slip, preventing the emergence of a single throughgoing fault that could attain structural maturity. Following the mainshock, field mapping revealed zones of distributed fractures within an approximately 28 km long and up to 800 m wide rupture zone (Dee *et al.*, 2021; Koehler *et al.*, 2021). This distributed deformation, together with the slow rupture velocity (on average 1.5 km/s; Liu *et al.*, 2021), extensive off-fault aftershocks (Ruhl *et al.*, 2021), and the weakly discernible neotectonic landforms indicative of long-term faulting (Dee *et al.*, 2021; Koehler *et al.*, 2021), also suggest that the MCRE may have ruptured a highly immature fault system.

Several studies have investigated the MCRE rupture kinematics using a variety of data and methods. Dee *et al.* (2021) and Koehler *et al.* (2021) collected detailed field observations of surface ruptures and secondary fissures. Bormann *et al.* (2021) rapidly deployed temporary seismic stations and captured near-field light to moderate magnitude aftershocks (M_L 4–5). Ruhl *et al.* (2021) relocated the seismicity of the MCRE sequence and inferred that the mainshock and aftershocks ruptured fault-fracture networks that merge at depth. Various geodetic datasets have been inverted for the mainshock fault geometry and slip distribution, including Interferometric Synthetic Aperture Radar (InSAR) interferograms and azimuth offsets, Global Navigation Satellite System (GNSS) displacements, and seismic waveforms (Zheng *et al.*, 2020; Cui *et al.*, 2021; Hammond *et al.*, 2021; Li *et al.*, 2021; Liu *et al.*, 2021; Sadeghi Chorsi *et al.*, 2021). These published models comprise one to three fault segments and suggest peak coseismic slip of between 0.6 and 1.7 m.

Our study builds on this previous work by integrating our own geodetic mainshock slip model, aftershock relocations and mechanisms, and new field observations into a single study. Our mainshock model is distinct from the previous ones in that model slip is restricted to seismogenic depths that are independently constrained using calibrated aftershock focal

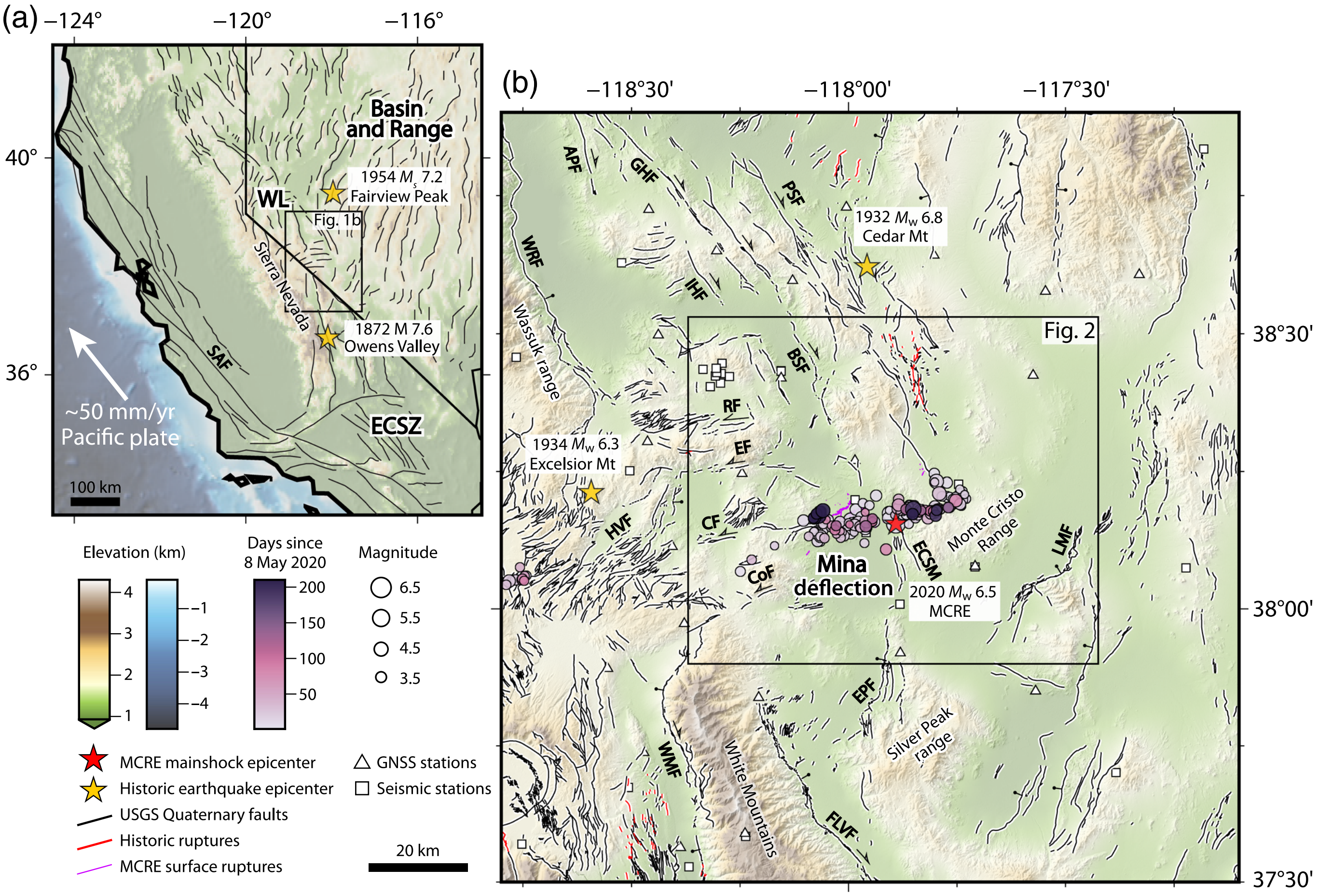

Figure 1. Tectonic setting of the 2020 Monte Cristo Range earthquake (MCRE). (a) Regional context of the eastern California shear zone (ECSZ) and Walker Lane (WL). (b) A zoom in of the Walker Lane. The red star is our relocated MCRE epicenter, and yellow stars indicate historic earthquake epicenters from the National Earthquake Information Center of the U.S. Geological Survey (USGS) and from Callaghan and Gianella (1935). The circles in panel (b) are relocated aftershocks of the MCRE, scaled with magnitude, and shaded with the number of days since 8 May 2020. Thin purple lines are the MCRE surface ruptures from Dee *et al.* (2021) and Koehler *et al.* (2021). Major faults (black lines) and historic ruptures (red lines) are from the USGS Quaternary fault and fold database (see Data and Resources): APF, Agai Pah fault; BSF, Benton Springs fault; CF, Candelaria fault; CoF, Coaldale fault; ECSM, Eastern Columbus Salt Marsh fault; EF, Excelsior fault; EPF, Emigrant Peak fault; FLVF, Fish Lake Valley fault; GHF, Gumdrop Hills fault; HVF, Huntoon Valley fault; IHF, Indian Head fault; LMF, Lone Mountain fault; PSF, Petrified Springs fault; RF, Rattlesnake fault; SAF, San Andreas fault; WMF, White Mountain fault; and WRF, Wassuk Range fault. The color version of this figure is available only in the electronic edition.

depths. Some of our field observations of surface cracking, including the first of pebble-clearing features in which pebbles and gravels are cleared unilaterally (on one side only) of surface cracks, also shed new light on the complex block motions within the fault zone. Our discussion of discrepancies between the findings of the different methods highlights the importance of incorporating geodetic, seismological, and field data to capture the full complexity of a rupture especially in a shattered crustal zone. Finally, we frame our results in the context of fault structural maturity, and show that various attributes of the MCRE are characteristic of rupture within an emergent and highly distributed fault system.

REGIONAL CONTEXT

The Walker Lane lies between the Sierra Nevada block and the Basin and Range extensional province (Locke *et al.*, 1940; Stewart and Ernst, 1988), and accommodates ~20% of the ~50 mm/yr dextral motion between the Pacific and North American plates at this latitude (Dokka and Travis, 1990; Bennett *et al.*, 2003). This shear is distributed across arrays of northwest-trending right-lateral strike-slip faults, north- to northeast-trending normal faults, and northeast-striking left-lateral strike-slip faults (Fig. 1), several of which have hosted large historic earthquakes, including the 1954 M_s 7.2 Fairview Peak, 1932 M_w 6.8 Cedar Mountain, and 1872 M 7.6 Owens Valley earthquakes (Hodgkinson *et al.*, 1996; Wesnousky, 2005).

The Mina deflection zone within the central Walker Lane disrupts the otherwise mostly northerly oriented structures with a suite of discontinuous east–west, left-lateral faults (Pierce *et al.*, 2021). These accommodate an ~25–60 km wide right step that helps transfer dextral slip between the longer, northwest-striking, right-lateral White Mountain and Fish Lake Valley fault zones to the southwest and the Benton Springs and Petried Springs faults to the northeast (Wesnousky, 2005; Lee *et al.*, 2009; DeLano *et al.*, 2019). Geologic, geomorphic, geodetic, and paleomagnetic studies suggest that they do so by rotating clockwise around vertical axes, opening small, triangular basins at the fault termini (Wesnousky, 2005; Petronis *et al.*, 2009; Rood *et al.*, 2011; Nagorsen-Rinke *et al.*, 2013; Bormann *et al.*, 2016; Grondin *et al.*, 2016; DeLano *et al.*, 2019; Pierce *et al.*, 2021). From north to south, the most conspicuous of these Mina deflection faults are the Rattlesnake, Excelsior, Candelaria, and Coaldale faults (Fig. 1), each of which is made up of numerous discrete segments that sum to lengths of up to ~20 km (Wesnousky, 2005). In general, the faults exhibit alternating north- and south-facing vertical scarps, geomorphic marker offsets, linear fault-bounded ridges, en echelon fractures and pressure ridges, and beheaded stream channels within bedrock and Quaternary alluvium, indicative of left-lateral and normal faulting (Wesnousky, 2005; Lee *et al.*, 2006). The only historic earthquake in this area is the 1934 M_w 6.3 Excelsior Mountain earthquake, which produced en echelon fissures and down-to-the-north vertical scarps along the Excelsior fault, consistent with left-lateral–normal slip (Callaghan and Gianella, 1935; Wesnousky, 2005).

The MCRE is the largest instrumentally recorded earthquake in the Mina deflection. The mainshock ruptured areas where east-trending Quaternary faults have not been mapped, as well as sections where the rupture projects into the northwest-striking Benton Springs and Petrified Springs faults in the north (Koehler *et al.*, 2021). In the west, the MCRE ruptured along strike (east) of the mapped Candelaria fault. Although there are no historic earthquakes along the Candelaria fault, it exhibits evidence for surface ruptures in the middle-to-late Holocene (Wesnousky, 2005), with a net left-lateral–normal slip of ~900 m since 2.8 Ma, measured from offset markers of Pliocene basalt, for a Quaternary slip rate of ~0.3 mm/yr (Speed and Cogbill, 1979).

DATA AND METHODOLOGY

Surface faulting observations

Surface rupture mapping. One of us (Ian Pierce) visited the MCRE area from 16 May (one day after the earthquake) to 7 June 2020, as part of a larger field team investigating surface faulting. The field observations described here are based upon and augment the subcentimeter resolution uncrewed aerial system (UAS) imagery, detailed surface rupture mapping, fault offset measurements, and surface crack orientation data collected by this team and published by Dee *et al.* (2021) and Koehler *et al.* (2021). We reinterpret these datasets in the context of our InSAR analysis of mainshock faulting (see the Mainshock Surface Ruptures and Fault Kinematics and Complexity Revealed by Combining Geodesy, Seismology, and Field Observations sections).

Paleoseismic trenching. During this fieldwork, one of us (Ian Pierce) also excavated an exploratory paleoseismic trench to seek evidence for any previous ruptures. The trench was sited along what appeared to us to be one of the pronounced MCRE surface ruptures and oriented perpendicular to their northeasterly trend. The 4.7 m x 0.9 m x 1.3 m deep trench was excavated by a backhoe, logged, and backfilled on the same day. Both the trench walls were photographed with a handheld camera, and an orthomosaic was created using Structure from Motion technique (see Data and Resources). No samples were collected from the trench.

Long-term fault offsets. We analyzed satellite multispectral imagery and digital topography to search for and quantify any geologic or geomorphic offsets indicative of long-term faulting or cumulative displacement (a proxy for structural maturity). Using a Sentinel-2B image acquired on 3 May 2022 (see Data and Resources), we generated false color imagery with band combinations 4-3-2 (natural color) and 12-11-2 (false color). We enhanced these with a standard deviation color stretch to highlight feature contrasts from which apparent cumulative offsets were derived. At fault scarp locations, we extracted topographic profiles from the U.S. Geological Survey (USGS) 3D Elevation Program 1/3 arc-sec (~10 m) seamless digital elevation model (DEM) to estimate vertical separations.

Geodetic slip modeling

InSAR and GNSS data and processing. We produced three six-day interferograms using Synthetic Aperture Radar (SAR) images acquired by the European Space Agency's C-band (wavelength 5.6 cm) Sentinel-1 satellites (see Data and Resources). The SAR images were obtained on four dates between 10 May 2020 and 17 May 2020 by two adjacent descending tracks and one ascending track (Table 1), offering three looking angles. The interferograms were processed with GAMMA software (Wegmüller *et al.*, 2016). We removed the topographic phase contribution using the 3 arc-sec (~90 m) Shuttle Radar Topography Mission (Farr and Kobrick, 2000) DEM (see Data and Resources). The interferograms were filtered using a power spectrum algorithm (Goldstein and Werner, 1998), unwrapped using the branch-cut algorithm, and georectified to the Universal Transverse Mercator coordinate system (UTM zone 11 N) with a 90 m pixel resolution (Fig. 2). Finally, we manually fixed unwrapping errors in areas that show spurious phase discontinuities, and carefully removed a few patches disconnected from the main interferogram and for which the unwrapping uncertainty is high.

We also collated regional GNSS coseismic offsets processed by the Nevada Geodetic Laboratory using their updated dataset released on 19 June 2020 (Blewitt *et al.*, 2018). The data comprise continuous GNSS stations belonging to the Mobile Array of GPS for Nevada Transtension (MAGNET), Network of the Americas, and other networks, which together provide a

TABLE 1
Details of the Interferometric Synthetic Aperture Radar Imagery Used to Model the 15 May 2020 Monte Cristo Range Earthquake

Interferogram	Track	Date 1	Date 2	LOS Incidence (°)	LOS Azimuth (°)
intf1	d144	10 May 2020	16 May 2020	33	281
intf2	d71	11 May 2020	17 May 2020	44	280
intf3	a64	10 May 2020	16 May 2020	41	80

Line-of-sight (LOS) incidence angles (from the vertical) and azimuths (degrees from north) are measured at the mainshock epicenter. Abbreviations: a, ascending track; d, descending track; and intf, interferogram.

typical station spacing of ~20 km across the study area (Fig. S1, available in the supplemental material to this article).

Uniform slip modeling. We solved first for the mainshock fault geometry and then for the slip distribution by jointly inverting the three unwrapped interferograms and the GNSS coseismic offsets, using a routine elastic dislocation procedure (e.g., Wright *et al.*, 1999) described in detail in the following. To prepare the data for inversion, the three interferograms were downsampled using a Quadtree algorithm (e.g., Jónsson *et al.*, 2002; Wright *et al.*, 2003) in which the sampling block size and variance threshold were adjusted such that each downsampled dataset comprised ~400–600 data points concentrated within areas of high phase gradient. We only modeled the 25 GNSS data points within the extent of the InSAR coverage, all within ~75 km of the mainshock epicenter (Fig. S1). We experimented with using horizontal and vertical offsets or only the horizontal ones; finding little difference in our results, our final model incorporates all the three components. Because the two descending interferograms share similar look angles, they are together weighted equally to the single ascending interferogram and the GNSS offset dataset.

We first estimated the fault location and geometry by assuming that the earthquake occurred along a rectangular fault plane in a uniform elastic half-space with Lamé constants λ and $\mu = 3.2 \times 10^{10}$ Pa. We solved the Okada (1985) equations using a downhill simplex algorithm (Press *et al.*, 1992) to obtain fault plane parameters that minimize misfits between data and model surface displacements. We solved for the fault strike, dip, rake, slip, center latitude and longitude, length, top depth, and bottom depth, but kept slip fixed at 0.5 m because of an expected trade-off with fault width. To ensure that a broad parameter space is searched and the global minimum misfit found, we used 500 Monte-Carlo restarts with starting parameters selected randomly from specified ranges (Wright *et al.*, 1999; Funning *et al.*, 2005; Elliott *et al.*, 2012). We started with broad parameter bounds centered upon values estimated directly from the InSAR imagery (strike, location, length, top depth) or from automated mainshock focal mechanisms (dip, rake, bottom depth), and then repeated the inversion with the narrower bounds given in Table S1 once a satisfactory, preliminary model fault geometry had emerged. For each interferogram, we also solved for three nuisance parameters: a translation in line-of-sight (LOS) to account for the uncertainty in LOS at the unwrapping reference point, and east–west and north–south gradients in LOS to account for residual orbital ramps.

We initially modeled the geodetic data with a single, uniform slip fault plane, but the resulting model interferograms did not visually fit the InSAR data well. Adding a second uniform slip plane provided a much better visual and numerical fit, with eastern and western model faults accounting for the distinct fringe patterns observed east and west of the epicenter (Fig. 2).

Distributed slip modeling. Having determined the fault geometry, we next solved for the slip distribution. We started by extending the two uniform slip model fault planes along strike and up- and down-dip to allow for the possibility of slip outside of the extents of the uniform slip model. Both ends of the western and eastern model faults were extended ~1 km along strike, and their bottom depths were increased to 14 km to allow for tapering of slip at the base of the seismogenic zone. This does not exceed 15 km—the local seismogenic thickness inferred from our relocated hypocenters, the deepest of which is 11 km ± 1–4 km (see the Hypocentral Relocations and Aftershock Distribution and Mechanisms sections). The extended model fault planes were then each divided into 2 km × 2 km subfault patches, and the slip distribution was estimated using a Laplacian smoothing operator (Wright *et al.*, 2004; Funning *et al.*, 2005) and a slip positivity constraint (Bro and De Jong, 1997). Following Wright *et al.* (2004), we chose a smoothing constant that maximizes the smoothness of the slip distribution without greatly increasing the model misfit. Full parameters of our final slip model are provided in Data file S1.

Seismological analysis

Hypocentral relocations. In addition to geodesy, we relocated the hypocenter locations of the mainshock and 196 well-recorded foreshock and aftershock events using the *mloc* multievent relocation software (Bergman and Solomon, 1990; Walker *et al.*, 2011; Karasözen *et al.*, 2019; Benz, 2021). This utilizes arrival-time data of multiple earthquake events recorded at multiple stations to minimize biases from unknown Earth velocity structure and thus obtain calibrated hypocenter

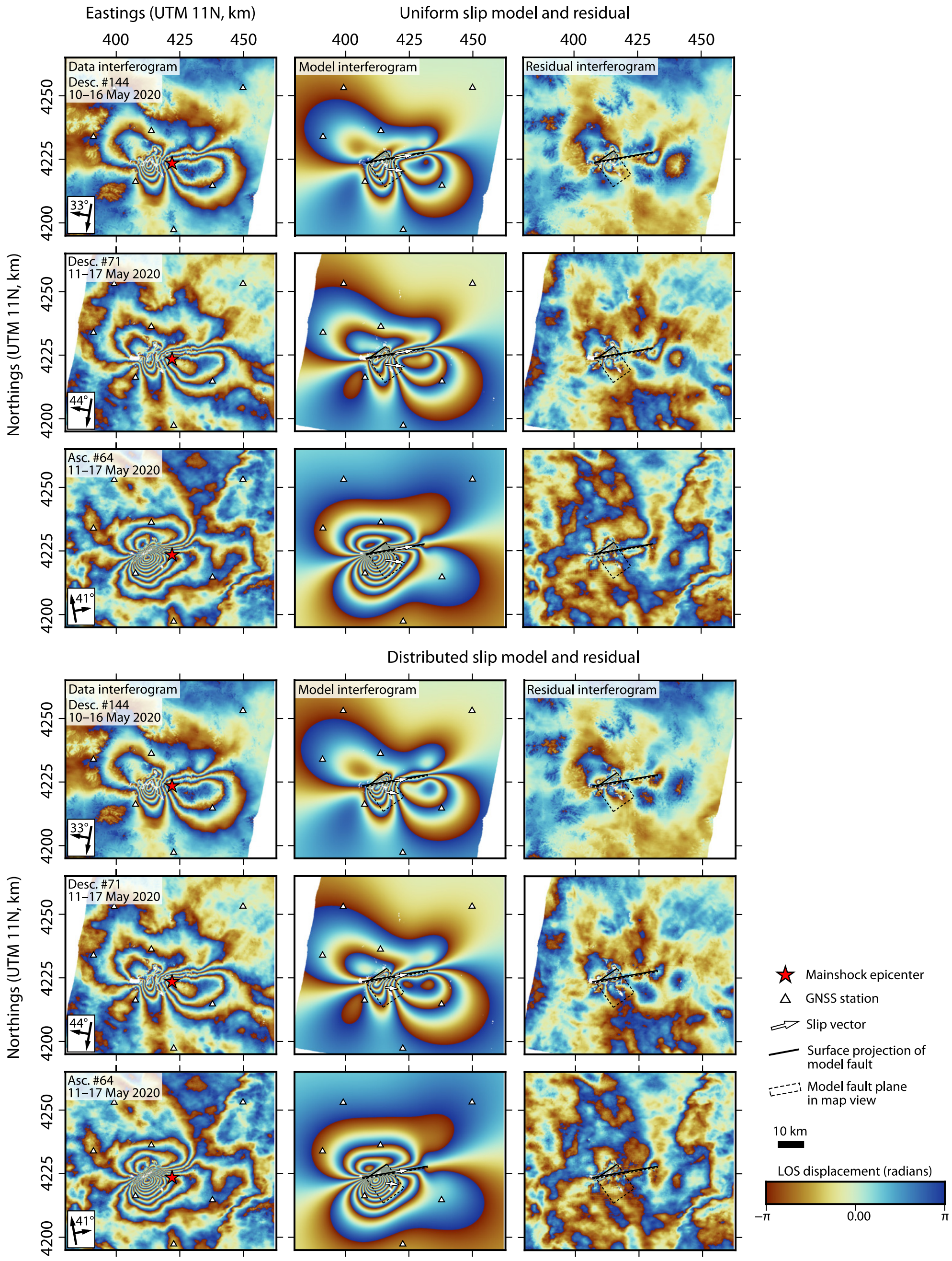

Figure 2. Observed, model, and residual wrapped interferograms of the uniform slip and distributed slip inversions. The satellite orbital tracks (asc., ascending; desc., descending) are followed by the track number and the interferogram date range. Satellite track and line-of-sight (LOS) azimuths are given as long and short vectors in the corner of the data interferograms, along with the incidence angle. The thick black lines indicate the surface projection of the model fault, the dashed box illustrates the model fault plane in map view, and the white arrows denote the slip vector of the hanging wall. The red star is the relocated mainshock epicenter, and the white triangles are nearby Global Navigation Satellite System (GNSS) stations. Unwrapped interferograms are provided in Figure S5. The color version of this figure is available only in the electronic edition.

parameters. We used arrival-time data gathered from the International Seismological Centre bulletin and the USGS Advanced National Seismic System Comprehensive Earthquake Catalog for well-recorded events from 8 May 2020 to 3 December 2020 (see Data and Resources).

Mloc adopts the hypocentroid decomposition algorithm, which separates the relocation into two inverse problems, for which tailored arrival-time data can be used. First, the program uses all available arrival-time data at all epicentral distances to solve for the relative locations of each hypocenter in the cluster. These cluster vectors connect each event to the hypocentroid—the geometric mean for all hypocenters (Fig. S2). Second, the algorithm calculates the absolute location of the hypocentroid and updates the absolute hypocenter locations of every event in the cluster using all the arrival times at close range. In our case, more than 4500 arrival-time readings at distances of less than 0.7° contributed to the absolute relocation step (Figs. S3 and S4). The high density of local recordings allowed us to solve for focal depth as a free parameter, though for some events we manually adjusted depths to better fit near-source or local-distance data. We utilized a bespoke regional velocity model for the crust and upper mantle, and the ak135 global model for below 120 km (Kennett *et al.*, 1995; Table S2). Our relocated hypocentral dataset is tabulated in Data file S2, and travel-time residuals are plotted in Figure S4.

Regional moment tensors (RMTs). Among the 197 relocated events, we also calculated RMT solutions for the mainshock and 89 best-recorded aftershocks. We modeled regional waveforms collected from the Incorporated Research Institutions for Seismology and the Nevada Seismological Laboratory at the University of Nevada, Reno, at distances of 0–500 km (see Data and Resources). For events M_w 5.0 or smaller, we used the whole seismograms, bandpass filtered at

~10–100 s. For events larger than M_w 5.0, we used W-phase waveforms filtered in the passband ~50–2000 s. We solved for the RMTs using the inversion methods, Green's functions, and central U.S. velocity model of Herrmann *et al.* (2011). To determine the best fit between observed and modeled waveforms, we assumed that a point source and the moment tensor components were grid searched at 1 km depth intervals. The dense regional station coverage provided well-constrained centroid depths. Further sensitivity testing revealed the other RMT parameters to be insensitive to perturbations of a few kilometers in centroid depth.

RESULTS

Mainshock surface ruptures

Field observations include variably oriented surface ruptures with discernible slip and measurable offset, and smaller cracks without clear kinematic indicators (Dee *et al.*, 2021; Koehler *et al.*, 2021). Surface ruptures have lengths of ~100–200 m to ~1–2 km but are heavily segmented with gaps and stepovers. Individual segments are mostly a few meters to tens of meters long, though a few reach lengths of >100 m. The surface cracks are mostly a few meters to tens of meters long, are distributed away from the main fault trace (up to ~500 m), and have larger variations in orientation than the surface ruptures (Fig. 3). In the eastern part of the rupture area, field observations of surface deformation are sparse and mostly located off the main eastern fault, as revealed by InSAR. This is consistent with our eastern InSAR–GNSS model fault, which shows a pronounced shallow slip deficit (SSD) (see the Mainshock Source Model and Mechanisms section). The longest alignment of surface ruptures is immediately south of and conjugate to the eastern model fault (Fig. 3a), and involves up to ~10 cm of right-lateral motion over a distance of ~1.2 km (Dee *et al.*, 2021; Koehler *et al.*, 2021).

Most of the observed surface ruptures and cracks lie within the western part of the mainshock fault zone and are the main focus of this section. There are two main alignments, both trending approximately northeast (Fig. 3a). The first, narrower alignment (referred to herein after as the "western fault zone") approximates the trace of the western InSAR–GNSS model fault over a distance of ~10 km, and accommodates up to ~10 cm of left lateral and ~7 cm of vertical motion (Fig. 3b,c). These motions are roughly consistent with our InSAR analysis, which supports up to ~10 cm of surficial, oblique (left-lateral–normal) slip along the southeast-dipping, western model fault (see the Mainshock Source Model and Mechanisms section). However, the vertical slip observed in the field exhibits a mix of down-to-the-southeast and down-to-the-northwest (DTNW) throw, indicating that the shallow faulting is more complex than our InSAR–GNSS model can resolve.

The second main alignment of fractures (referred to herein after as the "northern fault zone") lies ~1–3 km to the northwest of and subparallel to the western fault zone, and contains the largest discrete offset observed anywhere in the field (Fig. 3b,c). It comprises several discrete arrays of faults and cracks, distributed even more diffusely than in other areas, with thousands of individual fractures across a ~6 km × ~1 km zone. Though the overall trend is northeastward, individual fracture sets exhibit a wide variety of orientations. Where fault slip can be resolved, the kinematics are predominantly left lateral (with offsets of up to ~20 cm) and vertical DTNW (with throw of up to ~10 cm). Though this fault zone does not align with our InSAR–GNSS model faults, it is consistent with a minor discontinuity visible in the unwrapped interferograms (Fig. 4a,b). The sense of the LOS displacement discontinuity in the ascending interferogram supports that the left-lateral motion dominates over the vertical component across this northern fault zone.

Within the western and northern fault zones, many of the fractures also exhibit a clearing of loose pebbles or gravel from only one side of each crack (Fig. 4c–f). This phenomenon is particularly evident in which fractures break desert pavement surfaces and is generally absent from sandy surfaces. The width of the cleared zone is typically a few centimeters, large enough that the cleared side could be mapped from fine-resolution UAS imagery (Dee *et al.*, 2021; Koehler *et al.*, 2021; Fig. 4c). The side that is cleared is consistent within each fracture set but can vary between sets, illustrated by the tip of white triangles in Figure 4a. For example, fractures along the northern fault zone are predominantly cleared of pebbles to the southeast (upthrown) side. Only a few are bilaterally cleared. We interpret that the predominance of unilateral clearing may represent significantly higher ground acceleration on one side of each fracture during the rupture process, perhaps related to local rupture dynamics. We further discuss the importance of these fractures in the Fault Kinematics and Complexity Revealed by Combining Geodesy, Seismology, and Field Observations section.

Mainshock source model and mechanisms

Both ascending and descending interferograms contain clear coseismic fringe patterns, with a maximum LOS displacement of ~31 cm (away from the satellite) observed in the ascending data (Fig. 2, left column). The east–west orientation of the two largest, northern and southern fringe lobes, with differing sense of LOS displacement in the ascending and descending data, is consistent with predominantly east–west, left-lateral faulting. However, the presence of a third, more condensed southwestern lobe in the descending interferogram hints at some variation in the faulting mechanism. In this area, LOS of displacements are away from the satellite in both ascending and descending interferograms, consistent with localized subsidence (unwrapped interferograms are provided in Fig. S5).

Our modeling results further illuminate the complexity in fault geometry and mechanism. Our preferred two-fault inverse modeling reproduces the InSAR–GNSS data well (Fig. 2; Fig. S1),

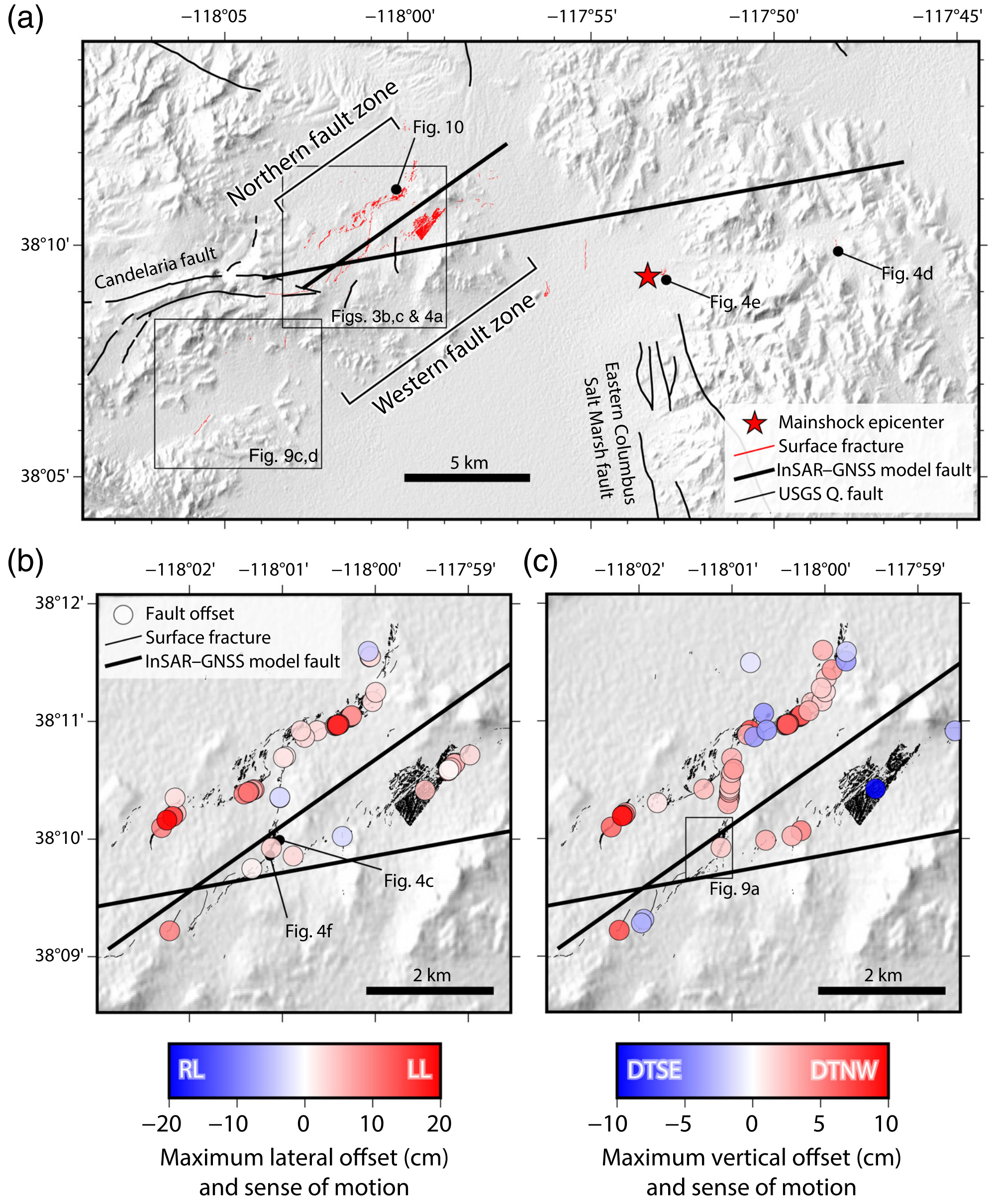

Figure 3. (a) Multidirectional hillshade map showing our calibrated relocated MCRE mainshock epicenter (red star), MCRE surface faulting and cracks mapped in the field (Dee *et al.*, 2021; Koehler *et al.*, 2021) (thin red lines), surface projections of our Interferometric Synthetic Aperture Radar (InSAR)–Global Navigation Satellite System model faults (thick black lines), and regional active faults as in the previous figures (thin black lines). Subpanels show (b) lateral and (c) vertical fault offsets measured in the field. Where several measurements were collected from the same locality, we take the maximum. The red- and blue-shaded circles represent the sense of motion, with the color gradient reflecting the amount of fault offset in centimeters. Positive values are assigned to left-lateral offsets in panel (b) and DTNW offsets in panel (c). Thin black lines are the near-field fractures, and thick black lines are InSAR–GNSS model fault surface projections. Abbreviations: DTNW, down to the northwest; DTSE, down to the southeast; LL, left lateral; and RL, right lateral. The color version of this figure is available only in the electronic edition.

with root mean square residual displacements of 0.6 and 0.8 cm in the uniform and distributed slip cases, respectively. In the uniform slip inversion in which the fault parameters are solved freely, the western and eastern model faults are 8.4 and 23.5 km long, respectively (Table 2). The eastern model fault strikes 80°, dips steeply southward at 88°, is predominantly left lateral with rake −4°, and crosses the entire rupture zone. The shorter western model fault crosses the eastern fault with strike 55°, dips more gently at 49° southeast, and exhibits oblique left-lateral–normal motion with rake −54°, explaining the subsidence inferred from the InSAR data. The western model fault terminates along strike from the eastern end of the Candelaria fault (Fig. 3a), but neither of the model faults align with the previously mapped structures. Our model slip distribution shows that of the total geodetic moment of 6.1×10^{18} Nm, ~70% occurs on the eastern model fault and ~30% on the western one. Maximum slip of 1.0 m occurs on the eastern fault at 8–10 km depth, but peak slip on the western fault of 0.7 m is much shallower at 3–4.5 km (Table 2). Both the model faults exhibit a clear SSD, in which only up to 0.1 m of model slip reaches the shallowest subfaults (discussed further in the SSD in the MCRE section).

We estimate model uncertainties and trade-offs by assessing the 500 Monte Carlo outputs from the uniform slip inversion (Figs. S6 and S7). Dip and rake are the two most interdependent parameters, whereas other parameters are generally clustered and do not strongly trade-off with each other. Inversion solutions with root mean square residual displacements of less than 0.9 cm (i.e., within ~10% of the global minimum misfit) are used to estimate standard deviations for each parameter. These indicate that western and eastern model fault strike varies by ±8° and ±1° (one standard deviation), respectively, dip by ±2° and ±3°, rake by ±7° and ±1°, easting by ±1 and ±2 km, northing both by ±0.3 km, fault length by ±0.3 and ±2 km, top depth by ±0.1 and ±0.2 km, and bottom depth both by ±2 km.

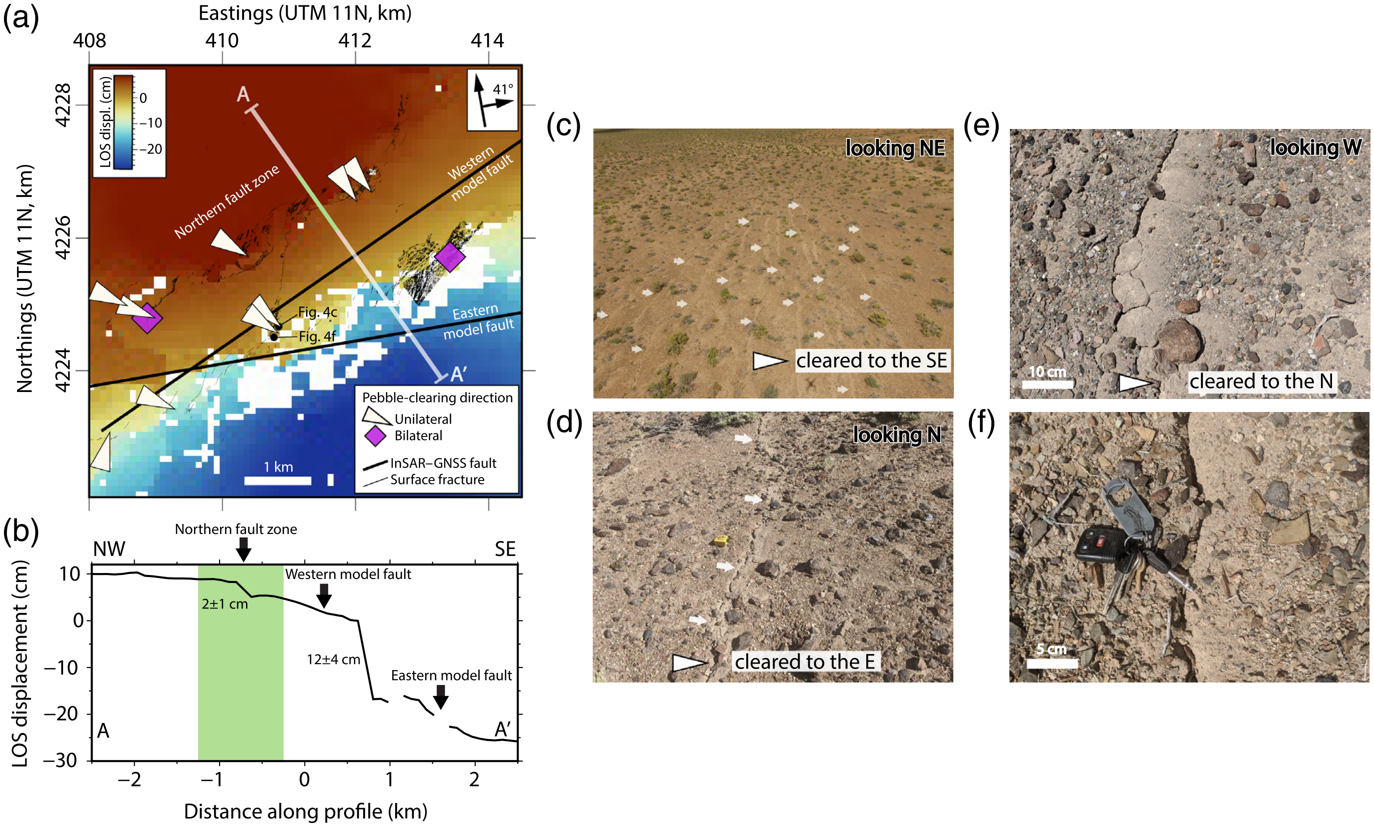

Figure 4. Photos of pebble-clearing phenomena from cracks and its direction of clearing. (a) Unwrapped ascending interferogram of the western MCRE rupture area showing the MCRE fault offsets and cracks mapped in the field (Dee *et al.*, 2021; Koehler *et al.*, 2021) (thin black lines), model faults (thick black lines), and pebble-clearing orientation (symbols). The direction to which the sediments are cleared are represented by white triangles (unilateral, cleared on only one side) and magenta diamonds (bilateral, cleared on both sides); triangle tips point to the cleared side or upthrown direction of the cracks. (b) Transect of unwrapped LOS displacements along A–A′ in panel (a). The shaded area illustrates the subtle LOS displacement discontinuity that colocates with the northern fault zone. (c) Oblique uncrewed aerial system (UAS) view looking northeast of a crack field with clearings on the southeast side of each crack indicated by white arrows. (d) Photo looking north, with a crack cleared to the east (tape measure for scale). (e) Close-up photo looking west, with a crack cleared to the north. (f) Close-up of crack showing clearing of loose materials on one side of the crack. Geographic coordinates of panels (c)–(f) are as follows: (38.1657° N, 118.0184° W), (38.1658° N, 117.8060° W), (38.1562° N, 117.8840° W), and (38.1641° N, 118.0190° W). The color version of this figure is available only in the electronic edition.

We conducted some additional tests to scrutinize further two of the more interesting aspects of our modeling results. The first of these is that the two model faults obliquely cross each other—an unusual attribute if real. To test whether this crossing pattern is robust, we repeated the uniform slip inversion but with the geometry of the eastern model fault fixed to force its termination against the western fault (Fig. S8). Uniform slip inversion of this configuration leaves large residual displacements at the fault intersection and the outer ends, showing that two nonintersecting faults cannot explain the InSAR data and suggesting that this unusual geometry is real.

The second interesting aspect of our modeling results is that the data are reproduced well without the need for a model fault along the northern fault zone. However, we explored whether a three fault model may explain the InSAR data better still, in particular, the subtle LOS displacement discontinuity observed across the northern fault zone, which our two fault model cannot emulate (Fig. 4a,b). To do so, we first fixed all parameters of the western and eastern model faults with their best uniform slip solutions from Table 2 (except the dip, rake, and bottom depth of the western segment). We then added a third, northern model fault to account for the northern fault zone, fixing several of its own parameters: its strike of 54° or 234°, center points and length of 6 km are chosen to approximate the mapped fractures, and its top depth of 0 km accounts for surface rupturing (Table S1). Finally, we solved for the northern fault dip, rake, bottom depth, and slip, with each given broad parameter bounds for the algorithm to search for the lowest misfit. The inversion results match but do not improve upon the 0.8 cm misfit of the simpler two-fault model (Fig. 5, second column). We obtain a similar moment of 5.6×10^{18} Nm, but with 7 cm of right-lateral–normal slip (rake = −138°) on the northern fault (Table S3), opposite in sense to the left-lateral field offsets. We further experimented with adjusted inversion configurations, but none yielded stable results that agreed with field or seismological observations.

TABLE 2
Parameters of Our Preferred, Two Fault Interferometric Synthetic Aperture Radar and Global Navigation Satellite System Uniform and Distributed Slip Models

Model Fault	Easting (km)	Northing (km)	Strike (°)	Dip (°)	Rake (°)	Length (km)	Width (km)	Top Depth (km)	Bottom Depth (km)	Moment (× 10^{18} Nm)	Peak Slip (m)	Peak Slip Depth (km)
Western	412.292	4225.944	55	49	−54	8.4, 10*	15.8, 18.0*	1.3, 0*	13.2, 13.5*	2.1, 1.9*	0.5, 0.7*	3.8*
Eastern	419.401	4225.717	80	88	−4	23.5, 26*	9.0, 14.0*	2.0, 0*	11.0, 14.0*	3.4, 4.1*	0.5, 1.0*	9.0*

Easting and northing refer to the center of the model fault surface projection in the Universal Transverse Mercator zone 11 N coordinates. The peak slip depth refers to the central depth of the peak slip subfault patch. The full slip distribution is tabulated in Data file S1.
*The distribute slip model parameters that changed from the uniform slip.

This difficulty might arise because a rectangular fault plane poorly fits the sinusoidal trace of the northern fault zone (Fig. 3a), or because the near-field InSAR data along the northern fault zone exhibit a relatively gradual phase gradient resulting in fewer downsampled InSAR data points for the inversion. We overcame this challenge by generating a suite of uniform slip forward models with varying geometries for the northern model fault: northwest-dipping left-lateral–normal, southeast-dipping left-lateral–reverse, and a vertical fault with left-lateral–dip-slip motion (Table S3). Slip was fixed to 10 cm, the median offset measured in the field. Results suggest that a vertical northern fault with left-lateral oblique motion best reproduces the InSAR data, though it does not fully match the observation (Fig. 5, last three columns). We discuss this geometry further in the Fault Kinematics and Complexity Revealed by Combining Geodesy, Seismology, and Field Observations section.

Our seismological analyses reveal additional characteristics of the mainshock rupture. The relocated, calibrated mainshock hypocenter is at 9 km depth on the eastern model fault plane (Fig. 6a), indicating that the earthquake ruptured bilaterally and mostly up dip. The *W*-phase moment tensor is predominantly strike-slip but exhibits a significant non-double couple component, broadly consistent with the orientation and kinematics of our InSAR fault model (Fig. 7). The *W*-phase centroid depth of 11 km is a little below the peak slip depth in our InSAR–GNSS model of 8–10 km (Fig. S9; Data file S3), and the *W*-phase moment of 6.8×10^{18} Nm is ~10% larger than (and likely within error of) our geodetic moment.

Aftershock distribution and mechanisms

Relocated aftershock hypocenters are scattered along a ~34 km long, approximately east-northeast trend, and span a focal depth range of 1–11 km with the greatest concentration at ~4–9 km (Fig. 7). Individual hypocenters have typical, formal uncertainties of ~0.4–0.6 km in epicentral coordinates (the average lengths of the short and long semiaxes of the 90% confidence ellipse) and estimated uncertainties of ±1–4 km in focal depth. RMT centroid depths are generally in close agreement (Fig. S9), but extend slightly deeper to 15 km. We conservatively estimated centroid depth uncertainties to be ~5 km, so we do not view the differences with focal depths to be significant. However, we consider the focal depths most reliable on the basis of their smaller uncertainties and overall narrower range.

The relocated aftershocks approximate the trend of the InSAR–GNSS model faults but are concentrated mostly to the south of the model fault surface projections. This is especially evident for the western model fault, with aftershocks reaching as far as 4–5 km southeast of its surface trace, consistent with the southeastward dip inferred from InSAR modeling. However, the aftershock map (Fig. 7a) and cross sections (Fig. 7b,c) both reveal numerous events up to several kilometers from the mainshock model faulting. Two clusters of off-fault aftershocks are located at both ends of the mainshock rupture. Other clusters are distributed along approximately northwest–southeast trends, conjugate to the mainshock faulting.

The aftershocks exhibit a mix of strike-slip and normal RMT mechanisms, many of them with east-northeast-trending nodal planes (Fig. 7a; Fig. S10). In the eastern rupture area, most aftershock mechanisms are predominantly strike-slip with east-northeast-trending left-lateral nodal planes and therefore roughly consistent with our InSAR–GNSS model. However, based on the presence of conjugate trends in relocated epicenters and field observations of scattered right-lateral offsets in this region, we interpret that some of these aftershocks involve north-northwest-striking right-lateral faults. We also observe many aftershocks with pronounced non-double couple components. Like the mainshock, these smaller aftershocks may have involved multiple faults of differing kinematics that sum to a non-double couple mechanism.

In the western rupture area, there is a wider mix of aftershock mechanisms including pure normal, oblique-normal, and strike-slip faulting. The normal mechanisms are concentrated near the western end of the rupture, are relatively shallow, and mostly involve northeast-trending nodal planes slightly oblique to the western model fault. The strike-slip mechanisms are concentrated near the eastern half of the

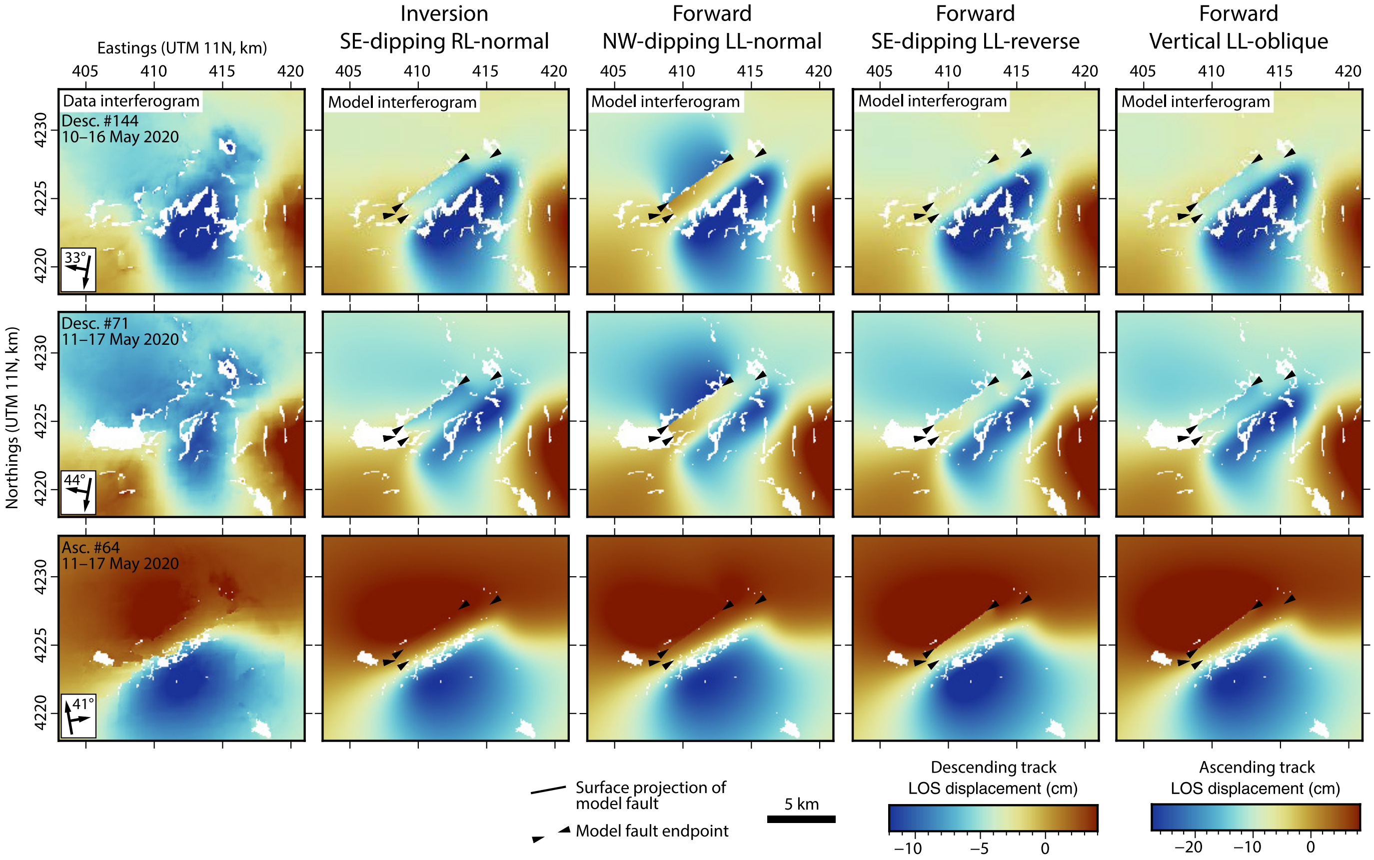

Figure 5. Observed and model interferograms in the western MCRE rupture zone, showing the addition of a third, northern model fault along the northern fault zone. The left column shows unwrapped data interferograms for the descending (upper and middle rows) and ascending (bottom row) tracks. Each remaining column shows an inverse or forward model interferogram for a particular northern model fault dip direction and slip sense (LL, left lateral; RL, right lateral). Black triangles mark the model fault end points so as to not obscure subtle phase discontinuities or the comparison with the data interferogram. The color version of this figure is available only in the electronic edition.

western model fault, are relatively deep, and have east-northeast-trending, left-lateral nodal planes. This hints that the real faulting at depth involves distinct strike-slip and normal faults, which are in close proximity but slightly oblique to one another. The crossing of our InSAR–GNSS eastern and western model faults supports this interpretation.

Comparisons with other geodetic slip models and seismological observations

We now compare our mainshock slip model with four previously published ones: Cui *et al.* (2021) and Li *et al.* (2021), who like us inverted InSAR and GNSS displacements to solve for the fault geometry and slip distribution, and Zheng *et al.* (2020) and Liu *et al.* (2021), who also incorporated a range of seismological data to solve for the kinematic rupture process. We also acknowledge the GNSS-derived uniform slip model of Hammond *et al.* (2021), however, this lacks the spatial resolution of the InSAR-based models and is excluded from our comparison.

Though the source geometries vary in detail between the five studies, all models including ours exhibit comparable kinematics: almost pure left-lateral slip on steep south-southeast-dipping faulting in the east and oblique left-lateral–normal slip on a more gently southeast-dipping structure in the west. Our eastern model fault dip of 88° is comparable to three of the other studies (78°–83°) but steeper than the dip obtained by Cui *et al.* (2021) of 65°. Our eastern fault length of 26 km is also consistent with three of the other models (26–28 km) but longer than the Li *et al.* (2021) solution of 18 km. However, ours is the only model in which the eastern fault extends across the entire MCRE rupture zone and crosses the western model fault. This is slightly different from Zheng *et al.* (2020) and Cui *et al.* (2021), whose eastern model faults extend to approximately the center of the western segment, but more markedly different from Liu *et al.* (2021) and Li *et al.* (2021), whose model faults align end to end and form a right step, respectively.

In the western rupture area, our western model fault is similar to that of Zheng *et al.* (2020), Cui *et al.* (2021), and Li *et al.* (2021), and only Liu *et al.* (2021) subdivide this into two subfaults: one dipping steeply below ~5 km and one dipping gently above. Our western model fault dip of 49° is intermediate between the other models (40°–64°). However, our aftershock

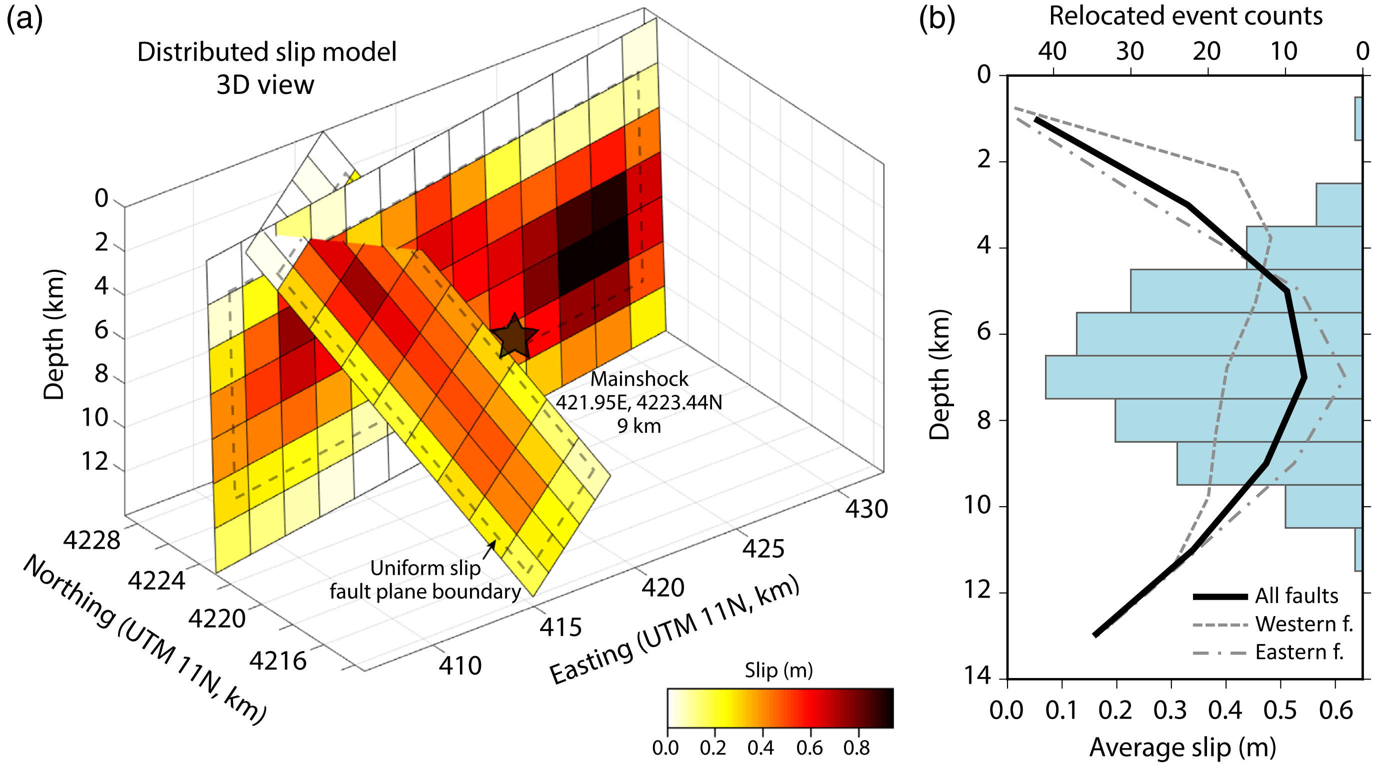

Figure 6. (a) Three-dimensional view of our preferred InSAR–GNSS distributed slip inverse model. Each subfault patch is 2 km×2 km, and the star shows our relocated mainshock hypocenter. Full parameters of each subfault patch are tabulated in Data file S1. Dashed lines show the fault plane boundary from our uniform slip inversion. (b) Model slip and aftershock depth profiles. Dashed and dashed-dotted gray lines show the average slip for each of the two model faults, plotted against the central depth of each row of subfaults. The thick black line shows the weighted average for all model faults, calculated by averaging all subfault patches within 2 km depth increments and plotting against the central depth of the bin range. The histogram shows the number of calibrated relocated earthquakes at each 1 km increment in focal depth. The color version of this figure is available only in the electronic edition.

relocations and mechanisms support overlapping northeast-striking normal faulting and east-northeast-striking left-lateral faulting in this area, where the other geodetic models have only a single, western model fault. Ours is therefore the only model in which the continuation of the eastern model fault across the western fault explains the aftershock distribution and its mixed kinematics. This highlights the importance of incorporating complementary aftershock datasets to illuminate the mainshock rupture in greater detail. Similarly, none of the InSAR–GNSS inverse models capture the ~6 km long northern fault zone, highlighting an important limitation in the spatial resolution of geodetic source inversions. It is only through forward modeling that we are able to characterize this structure, supporting left-lateral–normal slip on a vertical fault (Fig. 5).

Another significant difference between our model and the others is in the depth extents of coseismic slip. Whereas the bottom depths of our model fault planes are fixed to 14 km on the basis of the deepest, calibrated focal depths (11 ± 4 km; see the Aftershock Distribution and Mechanisms section), the other models have no such constraint with their model fault planes reaching depths of 21–24 km (Zheng *et al.*, 2020; Cui *et al.*, 2021; Li *et al.*, 2021; Liu *et al.*, 2021). In some cases, several centimeters of slip occur at the bottom of these planes (Fig. 8), well below the base of the seismogenic layer and despite slip below ~10 km being poorly resolved by available geodetic data (as acknowledged by Liu *et al.* [2021] in their checkerboard resolution test). Our shallower bottom depth likely explains why our model moment of 6.1×10^{18} Nm is 10%–20% smaller than that of Zheng *et al.* (2020) and Liu *et al.* (2021). This provides another example of how carefully calibrated aftershock data are useful in constraining mainshock properties.

There are also some more subtle differences in the model slip distributions. All of them show slip concentrated in two areas: a deeper (>5 km) patch on the eastern, left-lateral fault and a shallower (<5 km) patch on the western, oblique fault, and our peak slip of 1 m lies within the range of 0.6–1.7 m of the other four models. However, Zheng *et al.* (2020), Cui *et al.* (2021), and Li *et al.* (2021) place the greatest slip on the western fault at ~3–5 km depth, whereas we and Liu *et al.* (2021) place it on the eastern fault at ~6–10 km depth (Figs. 6b and 8a). All the five models display a pronounced SSD (Fig. 8b). Most of our shallowest row of subfault patches contains no model slip (Fig. 6a), consistent with Zheng *et al.* (2020) and Li *et al.* (2021) but in contrast to Liu *et al.* (2021) and Cui *et al.* (2021), whose each model has surface slip of up

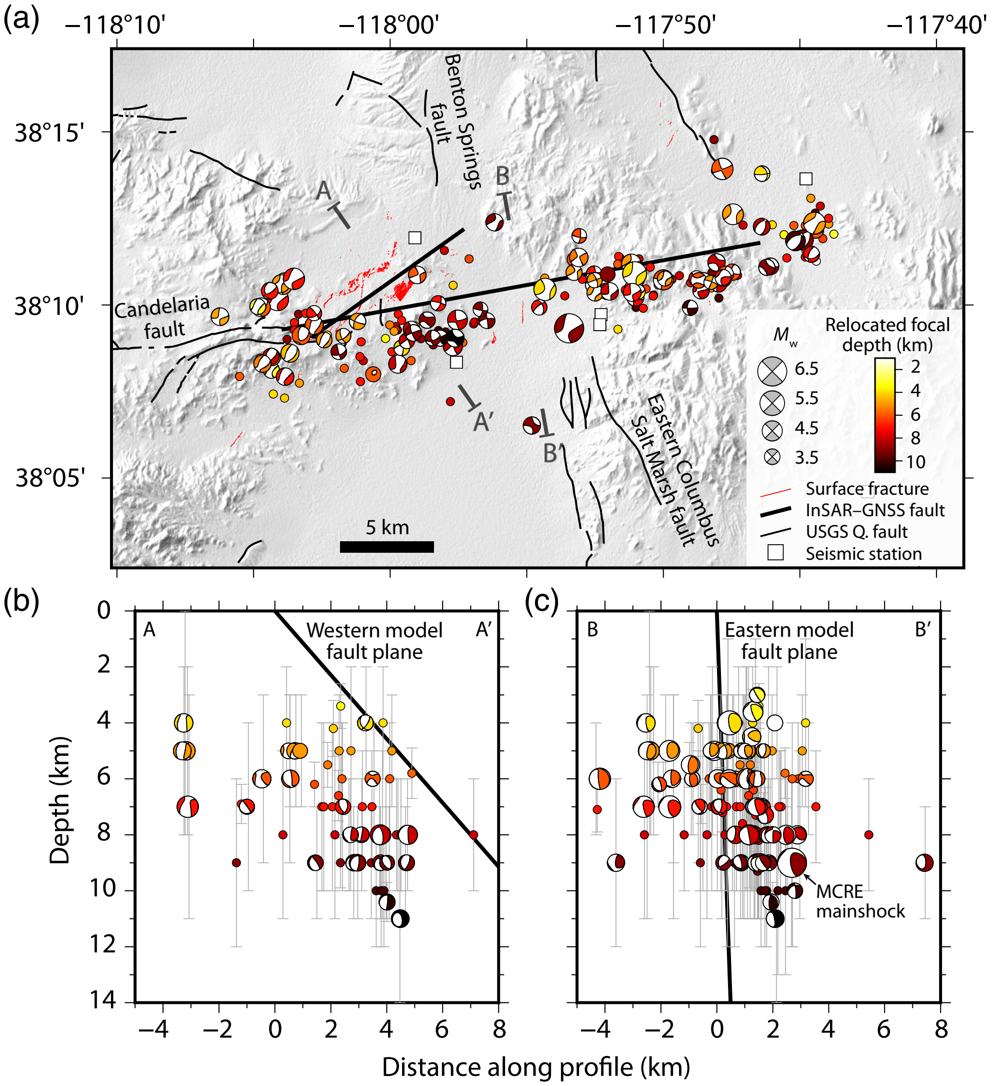

Figure 7. (a) Multidirectional hillshade map showing the relocated hypocenters and their focal mechanisms were available, plotted and colored by calibrated focal depth. Focal mechanisms are lower hemisphere projections scaled by moment magnitude. Smaller circles are events that are too small for waveform modeling ($M_w < 3.5$) plotted without any magnitude scaling. The thick black lines indicate the surface projection of the two model faults, thin black lines are the U.S. Quaternary faults, and thin red lines are the MCRE surface ruptures (Dee *et al.*, 2021; Koehler *et al.*, 2021). The black T-shape lines denote the cross-section transects, and squares indicate close-in seismic stations. (b,c) Cross-sectional views of the relocated hypocenters and focal mechanisms, plotted by calibrated focal depth with its uncertainties (Data file S2). Earthquakes are included where they lie within 5 (panel (b)) or 13 km (panel (c)) of the cross-section lines on panel (a). Focal mechanisms are back-hemisphere projections scaled by moment magnitude and, similar to panel (a), smaller circles are the remaining relocated hypocenters without mechanisms. Thick black lines are cross sections of the western (panel (b)) and eastern model (panel (c)) faults. The color version of this figure is available only in the electronic edition.

to ~0.4 m, greater than observed field offsets. We return to the SSD in the SSD in the MCRE section.

Finally, we compare our seismological results with those from Ruhl *et al.* (2021), which also incorporated eight temporary seismic stations deployed soon after the mainshock (Bormann *et al.*, 2021). They located and then relocated (with waveform-based double-differencing) ~18,000 events from 1 January to 31 August 2020, and used regional waveform modeling to estimate 128 moment tensors including for the mainshock. For the mainshock, their double-difference-based depth is 3.7 km, but their waveform model is 8.0 km, consistent with our InSAR peak slip at 8–10 km and within error of our own *W*-phase centroid depth of 11 km. Their best double-couple approximation of the fault plane shares the same strike, and agrees to within 7° in dip and rake with ours. However, their mechanism has a higher double-couple percentage (>95% vs. ~68%). Their relocated aftershocks are distributed almost exclusively above 12 km, in close agreement with our arrival-time-based calibrated focal depth range (up to 11 km) and a little shallower than our RMT centroid depth range (up to 15 km). Their aftershock moment tensors include a wide variety of strike-slip and normal mechanisms, similar to ours. In cross-sectional view, their denser, double-difference relocated aftershock clouds exhibit clear alignments that are not apparent in our own sparser data. These include structures that appear to align with our InSAR–GNSS model faults. For example, a transect across the central rupture zone reveals distinct shallow, ~60° dipping and deep, subvertical structures (fig. 5e in Ruhl *et al.*, 2021), consistent with the geometry of mainshock slip in which our western and eastern model faults cross one another (Fig. 6a).

Evidence of previous ruptures and cumulative offset

Although our InSAR–GNSS model faults do not align with the previously mapped faults, we found some field evidence for prior faulting along the MCRE surface ruptures and along the surface projection of the model faults. At several locations within the western fault zone, we observed northeast-trending calcite-filled

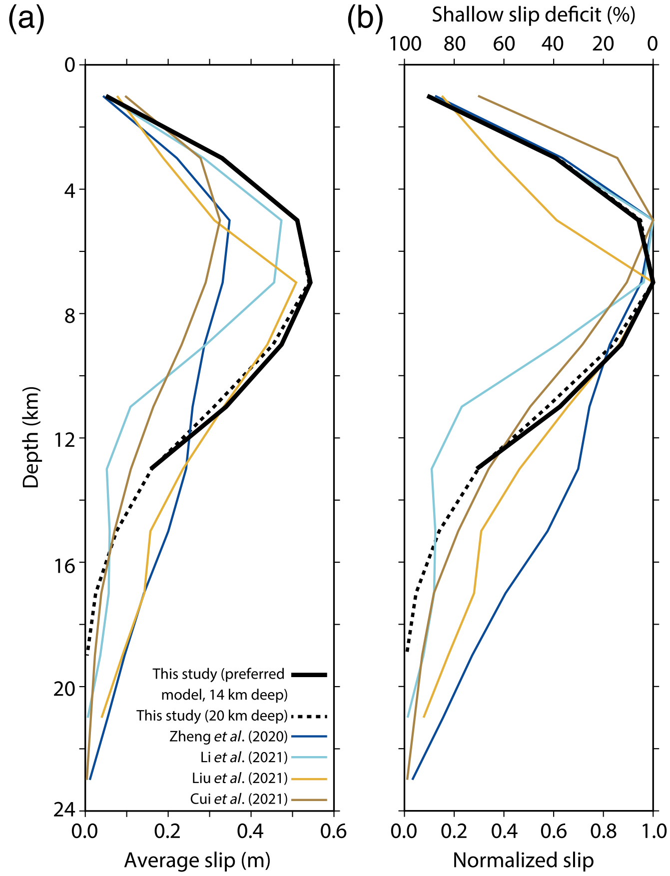

Figure 8. Comparison of MCRE geodetic model slip profiles from our article and other studies. (a) Average and (b) normalized slip in 2 km depth increments, demonstrating the pronounced shallow slip deficit (SSD). The deficit amount annotated along the top of panel (b) refers to the the shallowest data point of the profile and is equal to one minus the normalized slip of the surficial row of model subfault patches (0–2 km) expressed as a percentage. See the SSD in the MCRE section, for details of the slip profile calculations and further discussion. The color version of this figure is available only in the electronic edition.

cracks of a few to tens of centimeters in length (Fig. 9a,b). One of these is well exposed along a flat, scraped road surface. We interpret that the cracks formed in one or more previous earthquakes, and were subsequently cemented. Southwest of our western model fault, mapped MCRE surface ruptures with left-lateral and vertical DTNW offsets of 1–3 cm (Dee *et al.*, 2021; Koehler *et al.*, 2021) align at the foot of and thus appear to have reactivated an ∼1 km long, northwest-facing fault scarp—an opposite vertical slip sense to our western model fault (Fig. 9c–e). Our topographic profiles reveal vertical separations of 7 ± 2 m, indicative of several prior earthquakes along this structure. Otherwise, there is in general a limited expression of clear, neotectonic landforms such as scarps, channel offsets, or shutter ridges along the surface projections of our model faults.

Along the northern fault zone, our exploratory paleoseismic trench was sited where 8–9 cm left-lateral and 6–7 cm vertical DTNW surface offsets of the MCRE were measured (Dee *et al.*, 2021; Koehler *et al.*, 2021). The trenching reveals a sequence of subhorizontal fluvial and alluvial sands and gravels that are offset by faults and fissures (Fig. 10a,b). The three main stratigraphic units, from the lowest (oldest) to highest (youngest), include alluvial gravels from the trench floor to ∼0.4–0.5 m depth, bedded fluvial and alluvial sand and gravels from 0.4 to 0.2 m, and loose alluvium and silt capping the exposure (units A1, A2, and A3, respectively, in Fig. 10c,d). We observe at least five distinct vertical to subvertical fissures with openings up to ∼17 cm wide and one filled with gravels. Each fissure is marked by a white carbonate zone and alignments of pebbles that taper toward the trench floor. Three fissures disrupt unit A1 and are capped by A2, whereas the remaining two fissures extend to the surface. The surface-breaking fissures also contain white carbonate, but the carbonate is disrupted in these two fissures. We interpret the capped and carbonate-lined fissures to be evidence of prior surface rupturing earthquakes, and that the surface-breaking fissures result from both the 2020 MCRE and at least one prior earthquake. On the southern surface-breaking fissure, units A2–A3 alluvium contact has a 6–7 cm down-to-the-north offset, consistent with the 2020 MCRE surface fault offset adjacent to the trench (Fig. 10a,d). This vertical offset is also observed at the units A1–A2 boundary, but the contact irregularity there prevents an accurate quantification. The colocation of older and recent fissures demonstrates that the MCRE ruptured at least one preexisting fault structure.

The main fault trace of the MCRE trends approximately along strike from the Candelaria fault (Figs. 1 and 3a), which exhibits net, left-lateral–normal slip of ∼900 m since ∼3 Ma (Wesnousky, 2005). However, despite a rich and varied surface geology, our examination of digital topography and multispectral imagery (see the Long-term fault offsets section) yielded only two potential indicators of cumulative offset along the MCRE fault trace. Along the western model fault, outcrops of sedimentary rocks of the Candelaria (Triassic) and Palmetto (Ordovician) formations (Ferguson *et al.*, 1954) yield an apparent left-lateral offset of 600–700 m, using the interpreted geologic boundaries as piercing points (Fig. 11a–e). Along the eastern model fault, a ridge of Pliocene andesite (Ferguson *et al.*, 1953) exhibits 170 ± 40 m of apparent left-lateral offset, using projections of the ridgelines on either side of the fault to the inferred fault trace (Fig. 11f–j). However, both the estimates are tentative, given that thick alluvium obscures much of the geology in the west and the low relief of the ridge in the east.

DISCUSSION

Fault kinematics and complexity revealed by combining geodesy, seismology, and field observations

Overall, the MCRE and its aftershock sequence are consistent with the previous interpretations of active faulting in the Mina

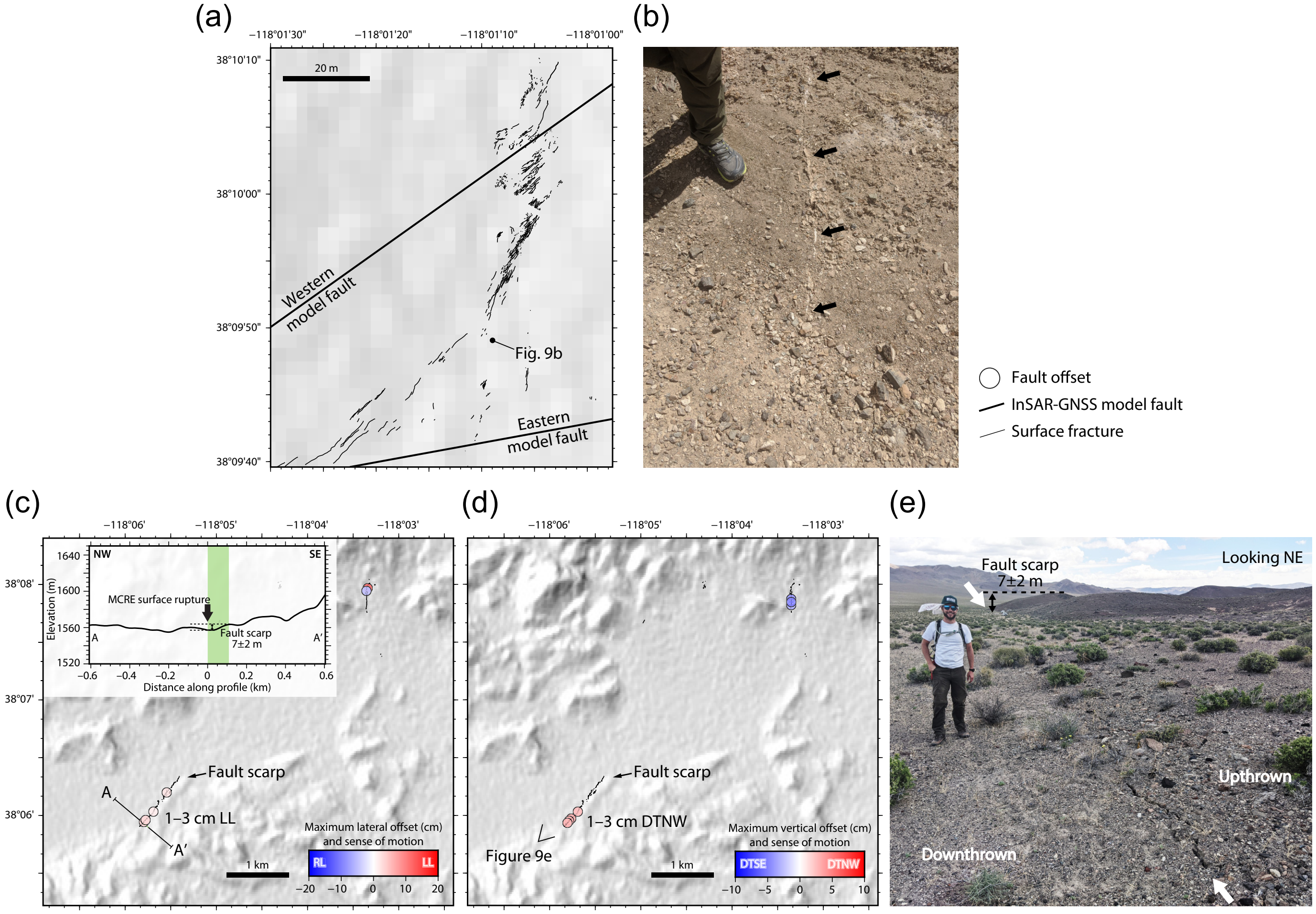

Figure 9. Hillshade topography maps and field photos showing evidence of the previous ruptures. (a) Hillshade topography of the western rupture zone illustrating the MCRE surface ruptures (thin black line), surface projection of the InSAR–GNSS model faults (thick black lines), and the (b) calcite-filled cracks denoted by the black arrows (38.1636° N, 118.0192° W). (c, d) Hillshade topography map southwest of the western model fault (see panel boundary in Fig. 3a) showing the MCRE surface ruptures along the foot of a northwest-facing fault scarp (38.0989° N, 118.0967° W), with their lateral (panel (c)) and vertical (panel (d)) fault offsets measured in the field (Dee *et al.*, 2021; Koehler *et al.*, 2021). The inset cross-section A–A′ in panel (c) illustrates the fault scarp vertical separation. The open arrow in panel (d) shows the approximate northeast viewing angle of (e) the field photo viewing along strike of the surface fractures, marked by the white arrows, next to the scarp. The color version of this figure is available only in the electronic edition.

deflection and its role in regional tectonics. The mix of left-lateral and left-lateral–normal faulting mimics the slip sense of other neighboring faults (Figs. 3 and 7), in particular, the well-studied Candelaria fault, which exhibits both vertical scarps and left-lateral geomorphic offsets (Wesnousky, 2005). Although oblique (left-lateral–normal) slip on the western, northeast-striking mainshock fault supports transtensional regional kinematic models (e.g., Oldow *et al.*, 2008), pure left-lateral slip on the eastern, east-striking mainshock fault is more consistent with the clockwise vertical-axis block rotation model for right-lateral shear transfer through the Mina deflection (Wesnousky, 2005). Normal faulting aftershock focal mechanisms located at the ends of the mainshock faulting also support the paired basins produced as a result of block rotation (Wesnousky, 2005; Fig. S10). In the long term, these block rotations may divert fault orientations away from those favorable to slip, promoting the formation of new faults and preventing older ones from becoming structurally mature (discussed further in the Characteristics of Structural Immaturity in the MCRE and Implications for Seismic Hazard Assessment section). The off-fault aftershock cluster at the western end of our model faults might be associated with energy radiated at the western rupture termination, reactivating the Candelaria and other local faults. We interpret that northwest-trending right-lateral strike-slip faults are also involved in the MCRE sequence; focal mechanisms conjugate to the eastern model faults project along strike with the major right-lateral Benton Springs and Petrified Springs faults, which help accommodate dextral shear transferred through the Mina deflection (Figs. 1 and 7; Wesnousky, 2005; DeLano *et al.*, 2019).

One of the most unique attributes of the MCRE is that the western and eastern mainshock faults cross one another, according to both our InSAR–GNSS modeling and aftershock hypocenters and focal mechanisms (Figs. 2 and 7). In most seismic

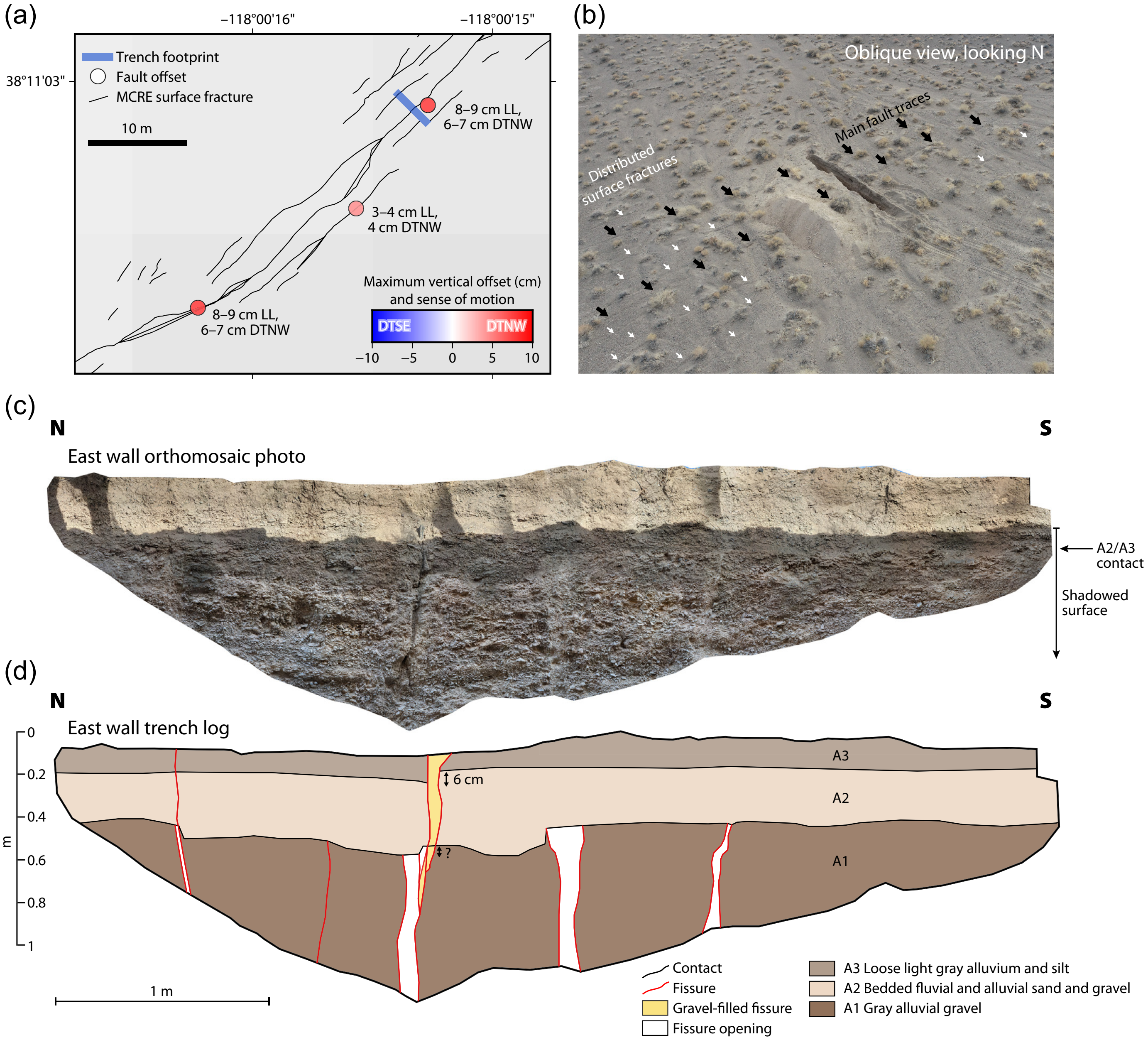

sequences with intersecting faults, the structures rupture sequentially in separate earthquakes, for example, the 1987 M_{s}6.2 and M_{s}6.6 Superstition Hills earthquakes and the 2019 M_{w}6.4 and M_{w}7.1 Ridgecrest earthquakes in California (Hudnut *et al.*, 1989; Barnhart *et al.*, 2019). In contrast, the MCRE ruptured two oblique cross faults in a single event. Examples of continental earthquakes in which conjugate faults ruptured together include the 1927 M_{w} 7.0 Kita Tango, Japan, and the 1992 M_{w} 6.5 Big Bear, California, earthquakes (Matsu'ura, 1977; Jones *et al.*, 1993). Dynamic simulations suggest that orthogonal faults are most likely to rupture together when both have high shear stress and when the initial slip direction toward the second fault is favorable for failure, leading to larger dynamic stress drops that promote rupture propagation across geometric complexities (Thatcher and Hill, 1991; Lozos, 2022). Our work motivates similar studies of obliquely crossing faults.

Figure 10. Paleoseismic trench across the northern fault zone of the MCRE surface rupture (38.1841° N, 118.0043° W). (a) Map view of the trench footprint, with the MCRE rupture trace and vertical fault offset measurements from Dee *et al.* (2021) and Koehler *et al.* (2021). (b) UAS oblique view of the trench looking north. The larger black arrows indicate the main continuous fault traces that cross the trench, and the smaller white arrows highlight the surface cracks concentrated at the southwest side of the trench. (c) Orthomosaic photo of the eastern trench wall. The darker brown shading is the shadowed surface, not to be confused with a unit contact. (d) Eastern wall trench log showing the three stratigraphic alluvium units, fissures, and offset measurements. The color version of this figure is available only in the electronic edition.

Our combination of near- and far-field surface deformation observations further reveals the complexity of the western MCRE kinematics. Our western InSAR–GNSS model fault dips

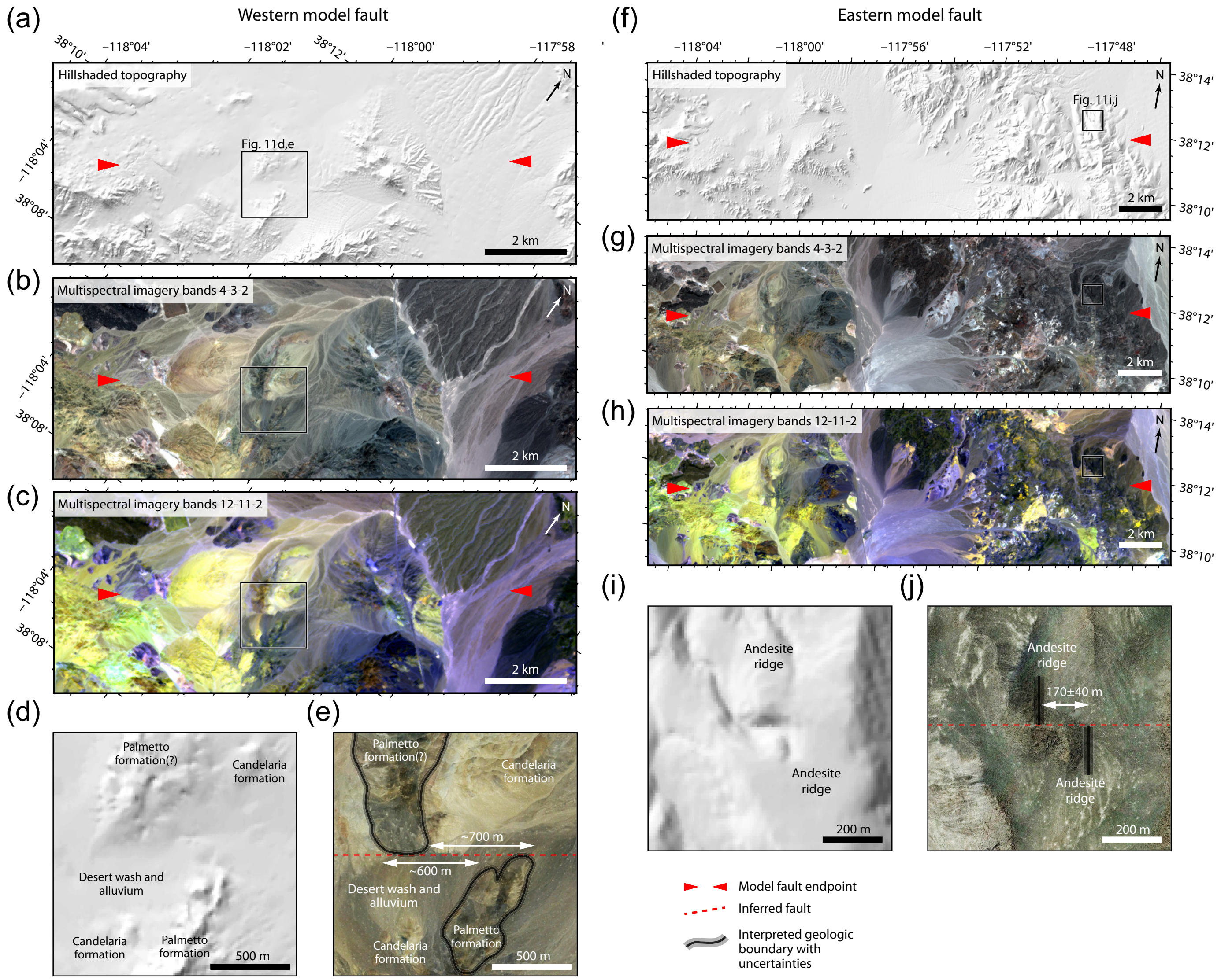

Figure 11. Hillshaded topography, multispectral imagery natural color bands 4-3-2, and geology composition bands 12-11-2 along the (a–c) western and (f–h) eastern InSAR–GNSS model faults, respectively (see the Hypocentral Relocations and Aftershock Distribution and Mechanisms sections, and Data and Resources). The red triangles indicate the model fault endpoints. The boxes denote boundaries of panels (d), (e), (i), and (j) showing potential geologic or geomorphic offset markers used to estimate the cumulative fault offset along the surface projection of the two model faults. The satellite photo in panels (e) and (j) is the 2016 Google Earth imagery with our own contrast enhancement. The color version of this figure is available only in the electronic edition.

southeastward with left-lateral–normal slip, and the unwrapped data interferogram shows a clear LOS displacement jump of 12 ± 4 cm (Fig. 4a,b). Approximately 1 km to the northwest, the northern fault zone displays a more subtle change in LOS displacement of 2 ± 1 cm across a 100–150 m distance, aligning with field observations of dominant left-lateral and vertical DTNW fault offsets (Fig. 3b,c), and surface cracks with preferential pebble-clearing to the southeast, also consistent with DTNW motion (Fig. 4a). The western and northern fault zones therefore have opposing vertical slip sense, with an upthrown block in between. Three competing structural configurations could potentially explain these observations. In the first configuration, the northern fault dips to the northwest and away from the western fault, accommodates left-lateral–normal slip, and forms a horst structure (Fig. 12a). However, the absence of normal-faulting aftershocks to the northwest or along strike of the northern fault zone implies that this may only be a very shallow structure (Fig. 7a). In the second configuration, the northern fault dips to the southeast, subparallel to the main fault, and slips in a left-lateral–reverse sense (Fig. 12b). However, we do not observe any reverse-sense aftershock focal mechanisms (Fig. 7b). In the third configuration, the northern fault is vertical and has left-lateral–oblique motion (Fig. 12c). This third scenario is supported by the focal mechanism cluster in the west; although located ∼2 km northwest of the northern fault zone, its steeply

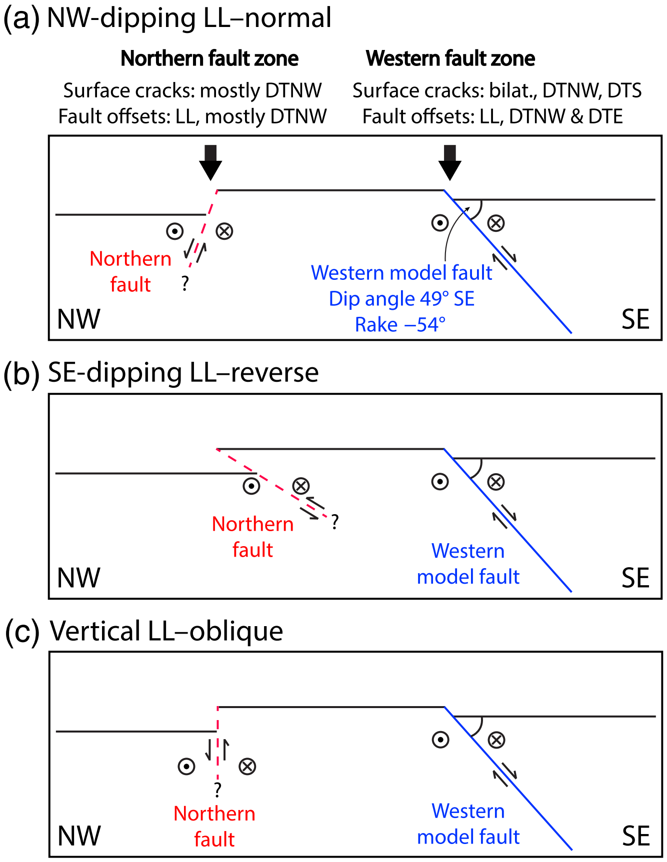

Figure 12. Three, competing, interpreted cross sections of the fault structure and kinematics in the western MCRE rupture area, inferred from near- and far-field observations. The southeast-dipping solid blue line is the InSAR-derived western model fault, and the dashed red line is the secondary, northern fault beneath the northern fault zone with its DTNW sense of throw. The secondary fault is interpreted as (a) a northwest-dipping left-lateral–normal, (b) a southeast-dipping left-lateral–reverse, and (c) a vertical left-lateral oblique fault. Abbreviations: bilat, bilateral; DTE, down to the east; DTNW, down to the northwest; DTS, down to the south; and LL, left lateral. The color version of this figure is available only in the electronic edition.

dipping geometry and kinematics match our proposed model (Fig. 7a,b), and by our vertical InSAR–GNSS forward model fault (Fig. 5, last column).

Along the secondary, northern fault, our geodetic, field, and seismological observations are only in partial agreement, reflecting each method's strengths and resolution in light of the geological complexity of the area. The poor depth resolvability of the shallowest aftershocks, (∼<4 km) a function of the lack of close-in seismic stations and the relocation method, illustrates the limitations of using regional seismograms to characterize the shallowest structures. However, aftershock relocations and mechanisms offer unique constraints on fault complexity within the deeper seismogenic layer. The shallower structures are likely the best represented by field observations, whereas InSAR best captures the mainshock rupture at larger length and depth scales. Furthermore, the geodetic and field data are, at first glance, contradictory: The major InSAR displacement discontinuity does not fully correspond to the largest fault offsets measured in the field. This likely reflects further complexity in the shallow fault zone as well as an abundance of off-fault deformation. Overall, our study demonstrates the importance of integrating geodesy, seismology, and field geology, perhaps along with other methods, to resolve the complexity of an earthquake sequence along and across strike and down dip, in which a single method on its own could easily lead to misinterpretation.

Characteristics of structural immaturity in the MCRE and implications for seismic hazard assessment

The MCRE ruptured faults that we interpret as being structurally immature, with few long-term geomorphic or geologic offsets discernible in the field or resolvable from satellite imagery and tentative cumulative offsets of only ∼600–700 m (see the Evidence of Previous Ruptures and Cumulative Offset section). Where known, other east-trending left-lateral strike-slip faults in the Mina deflection have slow slip rates of ∼0.3–0.4 mm/yr (Speed and Cogbill, 1979; Lee *et al.*, 2006)—another hallmark of structural immaturity. The weak manifestation of geomorphic offsets and slow individual fault slip rates likely reflect that vertical-axis crustal block rotations produce diffused, highly segmented faulting rather than a long, throughgoing fault.

The MCRE sequence, therefore, provides an example of rupture on a fault system of pronounced structural immaturity, and many of the rupture attributes may be characteristic of this. As described earlier, the mainshock geometry is complex for an earthquake of this magnitude, involving crossing faults with two distinct kinematic styles: subvertical left-lateral faulting in the east and inclined, left-lateral–normal faulting in the west. Moreover, broadly distributed fractures around the main fault traces reflect nonlocalized deformation commonly observed in immature fault zones (e.g., Zinke *et al.*, 2015). The off-fault distribution of aftershocks, their non-double couple focal mechanisms, and their wide variety of kinematics and orientations (Fig. 7) are further indications of a lack of a dominant throughgoing structure in the area. In addition, Liu *et al.* (2021) reported an average mainshock rupture velocity of ∼1.5 km/s—a relatively slow speed that is in agreement with other earthquakes along immature faults (e.g., Perrin *et al.*, 2016; Chounet *et al.*, 2018).

Our study also highlights the care needed for seismic hazard assessment in highly distributed, immature fault systems. For example, paleoseismic trenching would likely be required across a very large number faults for the full history of major earthquakes in this region to be captured but could still miss large events that did not rupture fully to the surface. Furthermore, simple fault length-magnitude scaling relations would not have anticipated an earthquake of the magnitude of the MCRE, and the characteristic earthquake model is probably inapplicable in regions of such diffuse faulting. Our work thus encourages seismic hazard calculations to consider that short segments may rupture together to generate large magnitudes, including unusual crossing-fault configurations.

SSD in the MCRE

Averaged over several earthquake cycles, the offset accommodated across a fault zone may be expected to be constant with depth. However, geodetic slip inversions of large earthquakes commonly exhibit peak model slip at depths of ~3–6 km with a reduction closer to the surface, termed the SSD (e.g., Simons *et al.*, 2002; Fialko *et al.*, 2005). The effect is often illustrated with a normalized slip profile (a plot of average slip against depth normalized against peak average slip) and parameterized as one minus the normalized slip of the surficial row of model slip patches (usually expressed as a percentage). Although absolute values depend in part upon whether or not near-field geodetic data are incorporated (Vallage *et al.*, 2015; Xu *et al.*, 2016; Marchandon *et al.*, 2018; Scott *et al.*, 2019), upon the assumed elastic structure (Amoruso *et al.*, 2004; Hearn and Bürgmann, 2005; Barbot *et al.*, 2008; Marchandon *et al.*, 2021), and upon other choices made in the modeling (Huang *et al.*, 2017; Ragon *et al.*, 2018; Li *et al.*, 2020), the general inference of SSDs in many large earthquakes is considered robust. Moreover, SSDs are also manifested in field measurements of surface slip along the primary fault trace (Dolan and Haravitch, 2014).

Several possible mechanisms causing SSD have been invoked, each with important implications for fault mechanics and earthquake physics. A switch to velocity-strengthening fault friction at shallow depths would naturally favor aseismic over seismic slip (Marone *et al.*, 1991; Marone, 1998). Damaged zones above a strike-slip fault may have a locally reduced seismic velocity, promoting inelastic off-fault deformation (Zhang *et al.*, 2009). Regions surrounding the shallow fault might undergo distributed deformation predominantly during the interseismic period, thereby accumulating little elastic strain (Fialko *et al.*, 2005; Lindsey *et al.*, 2014). Coseismic rupture might dissipate in the near surface through plastic yielding, particularly when near-surface materials are poorly consolidated (Kaneko and Fialko, 2011; Brooks *et al.*, 2017; Roten *et al.*, 2017). Alternatively, SSDs might simply reflect random differences in the depth extents of individual ruptures within the seismogenic zone (Berberian *et al.*, 2001; Yang and Yao, 2021; Yao and Yang, 2022). This would help explain why the largest events ($M_w > 7.5$), which are those most likely to fill the entire seismogenic layer and drive slip in any velocity-strengthening region, generally have reduced or absent SSDs (Tong *et al.*, 2010; Lauer *et al.*, 2020). Finally, SSDs might arise due to assumptions made in geodetic slip models, such as simplification of the Earth's elastic structure (Marchandon *et al.*, 2021), or due to near-fault image decorrelation leading to insufficient surface displacement data points to solve for shallow slip (Xu *et al.*, 2016).

Understanding what causes SSDs and how they might be compensated is vital for seismic hazard assessment, for a number of reasons. First, active fault mapping, slip rate estimations, and paleoseismic trenching all rely upon surface offsets; a pronounced SSD acts to obscure the link with earthquake faulting at depth (Dolan and Haravitch, 2014; Brooks *et al.*, 2017). Second, the suppression of near-surface slip can affect strong ground motions near the fault trace (Kaneko *et al.*, 2008; Pitarka *et al.*, 2009). Finally, there is the possibility that the slip deficit is removed by subsequent earthquakes centered at shallower depths (Berberian *et al.*, 2001; Jackson *et al.*, 2006; Elliott *et al.*, 2011; Mackenzie *et al.*, 2016). Alternatively, shortfalls in coseismic surface slip could be compensated through distributed coseismic deformation away from the main fault trace (Rockwell *et al.*, 2002; Simons *et al.*, 2002; Dolan and Haravitch, 2014; Zinke *et al.*, 2014; Milliner *et al.*, 2015; Scott *et al.*, 2018), as post-seismic afterslip (Fielding *et al.*, 2009) or as interseismic creep (Fialko *et al.*, 2005; Floyd *et al.*, 2016; Brooks *et al.*, 2017).

We now consider SSD in the MCRE in this context, using our own and other published InSAR models (Zheng *et al.*, 2020; Cui *et al.*, 2021; Li *et al.*, 2021; Liu *et al.*, 2021) and derived normalized slip profiles calculated using a common 2 km depth increment. Our own model has average surface slip of 0.05 m compared with peak average values of 0.54 m at 6–8 km depth (Fig. 8a), resulting in an SSD of 91% (Fig. 8b). SSDs of the other published models calculated in the same way span between 82% and 89%, except for a lower value of 70% obtained for the model of Cui *et al.* (2021). This general agreement implies that the large SSD inferred for the MCRE is robust.

The biggest difference between our normalized slip profiles and those of the other models is our shallower bottom depth, fixed to 14 km on the basis of relocated seismicity. We were, therefore, interested in the extent to which this could influence the calculated SSD. We test this effect by producing an alternative InSAR–GNSS model in which the fault planes are extended to ~20 km depth, but with an otherwise identical setup to our preferred model. The 20 km deep model yields average surficial slip of 0.05 m and peak average slip of 0.54 m at 6–8 km depth for a 91% SSD, values that are identical to our preferred 14 km deep model (Fig. 8). This suggests that varying the bottom depth does not influence the SSD. Rather, the main effect of increasing the bottom depth is to redistribute the deeper model slip: below 14 km, slip averages less than 0.08 m, and tapers toward zero at 20 km (Fig. 8a). However, the overall moment is only ~3% larger than our 14 km deep model.

The SSD in the MCRE may be compensated through several mechanisms. Shallow slip on the western fault might transfer in part to the nearby, subparallel northern fault zone, which is not represented in our InSAR–GNSS inverse model but where field offsets of up to ~20 cm were recorded (Dee *et al.*, 2021; Koehler *et al.*, 2021; Fig. 3). The northern fault zone might, therefore, account for up to around one quarter of SSD along our western model fault. Along the eastern fault, conjugate surface fractures with up to ~10 cm of slip can likewise only make up a small proportion of the SSD. However, given the broad deformation field, we expect that additional, unmapped fractures, folding, or volumetric strain could account for more of the absent shallow deformation. In addition, some amount of the SSD may have been removed by postseismic afterslip, of which only 1–2 days are captured in our interferograms. Hammond *et al.* (2021) compared coseismic and postseismic surface displacements across the MAGNET GNSS network within 70 km of the MCRE epicenter over a period of several months. They found that postseismic displacements mimicked coseismic displacement patterns at ~9%–51% of their values, but the long wavelength of this deformation suggests deep rather than shallow afterslip. Li *et al.* (2021) modeled a six-month InSAR time series and showed that rapid afterslip also occurred at shallow depths of 0–3 km with a peak slip of ~0.3 m. This likely recovered around another one-third of the missing slip, though later afterslip after the study period could potentially raise this contribution further. Any remaining shallow deformation is unlikely to be recovered by aftershocks or future earthquakes, because they would need to be centered at unusually shallow depths. Our calibrated relocated aftershocks mostly occur at depths greater than 4 km, exhibit small magnitudes, and are located off the main fault model (Fig. 7).

Are SSDs governed by fault structural maturity?

We have demonstrated that the MCRE occurred along a highly immature fault system and involved a pronounced SSD. In this final section, we consider whether these two characteristics are linked by assessing SSDs calculated from InSAR slip models of other continental, strike-slip earthquakes. This extends the work of Dolan and Haravitch (2014), who associated SSD with structural maturity by comparing published subsurface model slip distributions with field offsets of six large (M_w 7.1–7.9) continental strike-slip earthquakes. They found that for earthquake ruptures that occur on structurally mature faults (cumulative displacement ≥85 km), ~85%–95% of slip at depth reaches the surface (equivalent to a 5%–15% SSD), whereas only ~50%–60% does (a 40%–50% SSD) for ruptures on immature faults (cumulative displacement ≤25 km). This pattern holds regardless of their geometrical complexity; straight and continuous sections of immature faults still exhibit a pronounced SSD. Dolan and Haravitch (2014) interpret that the larger SSDs reflect more off-fault deformation at shallow depths for ruptures on immature faults, and that the smaller SSDs reflect more localized slip on a principle surface trace for ruptures on mature faults.

We investigate this further by comparing our normalized slip profile with those of 27 other continental strike-slip earthquakes modeled with InSAR (Fig. 13a; Table 3). We only consider earthquakes larger than M_w 6.4 because smaller events are less likely to rupture the full seismogenic layer. Many of the events have multiple published InSAR models, but we simplify our analysis by choosing one with a publicly available slip distribution (Fig. 8b would suggest that differences in profile shape are anyway likely to be modest). The normalized slip profiles are plotted according to the cumulative offset of the host fault, a common proxy for structural maturity, and separately by moment magnitude (Fig. 13b,c). We further extract the SSD for each earthquake from the shallowest data point of the slip profile, and compare the value with cumulative offset of the host fault and with moment magnitude (Fig. 13d,e).

Our results suggest that SSD does not consistently correlate with cumulative offset (Fig. 13d). For instance, the 2020 Elazığ earthquake ruptured the relatively mature East Anatolian fault (9–26 km net slip; Duman and Emre, 2013) but exhibits a modeled SSD of 85% (Pousse-Beltran *et al.*, 2020), whereas the 2019 Ridgecrest earthquakes ruptured very immature faults (<100 m; Gold *et al.*, 2021) with only ~30% SSD (Xu *et al.*, 2020). In contrast, moment magnitude does seem to correlate with SSD, with an R^2 value of 0.55 (Fig. 13e). Earthquakes of $M_w \geq 7.2$ produce small SSDs, mostly <10% and up to the maximum of 30% (in the 2021 Maduo earthquake). Earthquakes of $M_w < 7.2$ generally produce much larger SSDs, with half of them exceeding 80%, but also encompass a much broader range of values from negligible deficits (e.g., 1999 Hector Mine, 2017 Ormoc) to nearly complete ones (e.g., 2016 Muji, 2017 Ormoc, 2018 Kaktovik). In this context, the 91% SSD of the MCRE is more a function of its magnitude than its structural immaturity. This pattern can be explained in terms of the earthquake slip budget; moderate sized earthquakes will break to the surface most easily when the hypocenter is shallow but will otherwise leave large SSDs, whereas large earthquakes will rupture more fully to the surface whatever the nucleation depth (Lauer *et al.*, 2020; Yang and Yao, 2021; Yao and Yang, 2022).

CONCLUSIONS

Our geodetic, seismological, and field observations and modeling suggest that the MCRE ruptured two main structures, an eastern left-lateral fault and a western left-lateral–normal fault, which cross each other at an oblique angle, while also generating abundant off-fault deformation. Peak geodetic model slip of 1 m is buried at 8–10 km depth, and only up to 0.1 m of slip reaches the top 2 km of the crust (yielding an SSD of 91%), consistent with at most ~20 cm of fault offset mapped in the field. A third northern fault is required to account for mapped surface fractures with distinctive pebble-clearing patterns but is at the resolution limit of the InSAR–GNSS modeling. The intersecting fault geometry and distributed surface ruptures of the mainshock, the off-fault aftershocks with varying orientations and kinematics, and the limited expression of clear geomorphic features indicative of active faulting are indications that the MCRE ruptured an emergent zone of highly distributed faulting with

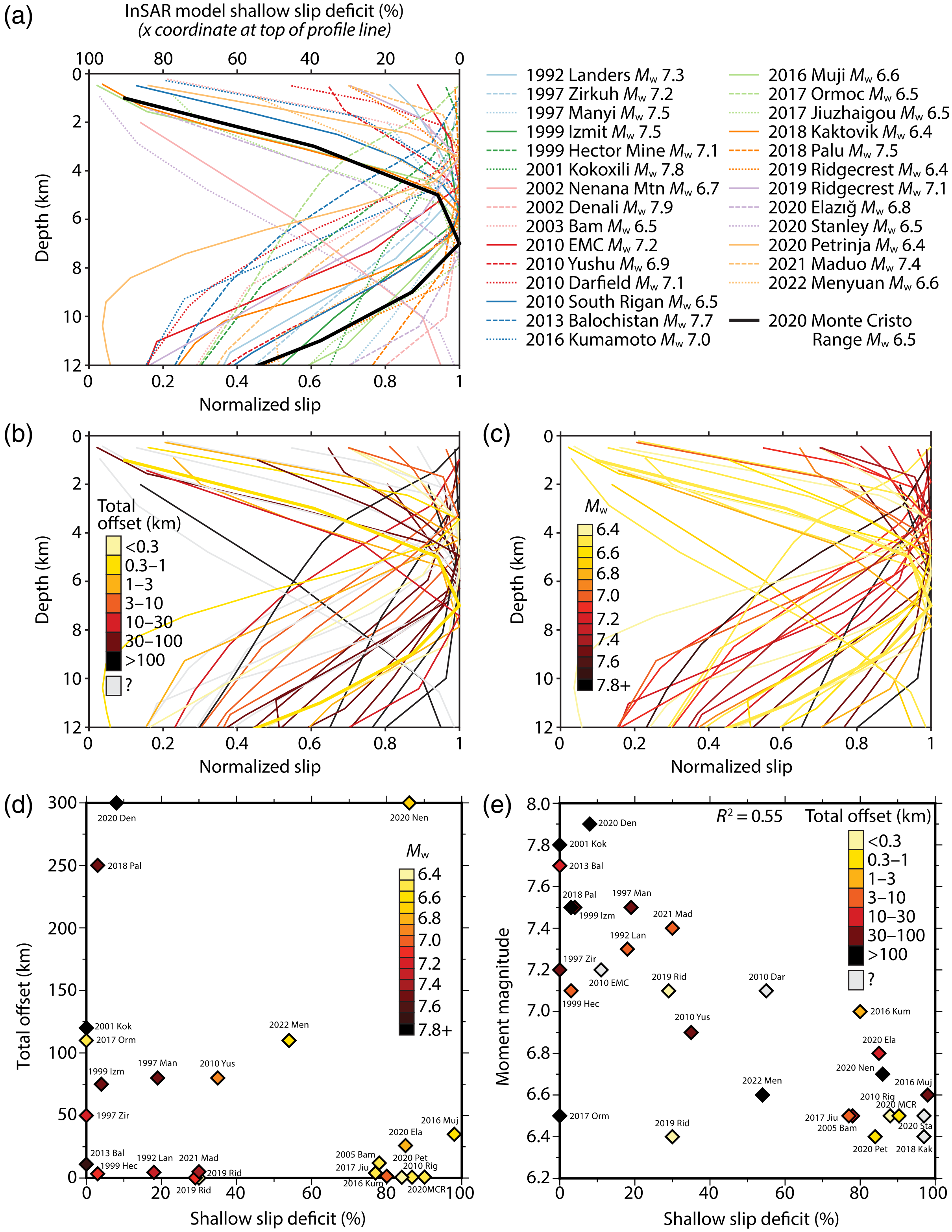

Figure 13. (a) Normalized slip profiles from InSAR-derived coseismic slip models of 28 large (M_w 6.4–7.9), predominantly strike-slip, continental earthquakes. Average slip in each layer of the model is normalized against whichever layer has the greatest average slip. The SSD annotated along the top of the panel refers to the shallowest data point of the profile and is equal to one minus the normalized slip of the surficial row of model subfault patches expressed as a percentage (e.g., Fialko *et al.*, 2005). InSAR model references are given in Table 3. (b) Normalized slip profiles colored by the total geological offset accumulated by the host fault (see Table 3 for offset values and references). (c) Normalized slip profiles colored by moment magnitude. (d,e) Scatter plots between SSD in percentage versus total offset in kilometers (colored by moment magnitude; panel (d)) and moment magnitude (colored by total offset; panel (e)). Earthquakes with unknown cumulative offsets on the host fault are excluded from panel (d). Data points are labeled with the event year and the first three letters of the event name, unless observed in Table 3. The color version of this figure is available only in the electronic edition.

TABLE 3
List of Earthquakes, Interferometric Synthetic Aperture Radar (InSAR) Model Shallow Slip Deficits (SSDs), and Cumulative, Geological Offsets for the Earthquakes Profiled in Figure 13

		InSAR Model SSD		Total Geological Offset	
Earthquake	**M_w**	**Value**	**Source**	**Value**	**Source**
1992 Landers	7.3	18%	Xu *et al.* (2016)*	3.1–4.6 km	Jachens (2002)
1997 Manyi	7.5	19%	Funning *et al.* (2007)	~20–80 km	Zhikun Ren, personal comm.
1997 Zirkuh	7.2	0%	Marchandon *et al.* (2018)*	~10–50 km	Richard Walker, personal comm.
1999 Izmit	7.5	4%	Çakir *et al.* (2003)	~4–75 km	Şengör *et al.* (2005)
1999 Hector Mine	7.1	3%	Xu *et al.* (2016)*	3.4 km	Jachens (2002)
2001 Kokoxili	7.8	0%	Lasserre *et al.* (2005)	100 ± 20 km	Fu and Awata (2007)
2002 Nenana Mtn†	6.7	86%	Wright *et al.* (2003)	~300 km	Eisbacher (1976)
2002 Denali	7.9	8%	Wright *et al.* (2004)	~300 km	Eisbacher (1976)
2003 Bam	6.5	78%	Fialko *et al.* (2005)	≪12 km	Jackson *et al.* (2006)
2010 EMC	7.2	11%	Xu *et al.* (2016)*	Mixed; unknown	Fletcher *et al.* (2014)
2010 Yushu	6.9	35%	Li *et al.* (2011)	39–80 km	Wang *et al.* (2008)
2010 Rigan	6.5	87%	Walker *et al.* (2013)	Probably small	Walker *et al.* (2013)
2010 Darfield	7.1	55%	Elliott *et al.* (2012)	Unknown	Jongens *et al.* (2012)
2013 Balochistan	7.7	0%	Lauer *et al.* (2020)*	~11 km	Zinke *et al.* (2014)
2016 Kumamoto	7.0	80%	Scott *et al.* (2019)*	800–1400 m	Scott *et al.* (2018)
2016 Muji	6.6	98%	Feng *et al.* (2017)	~30–35 km	Li Tao, personal comm.
2017 Ormoc	6.5	0%	Yang *et al.* (2018)	~110 km	Cole *et al.* (1989)
2017 Jiuzhaigou	6.5	77%	Li *et al.* (2020)	1–4 km	Li *et al.* (2019)
2018 Kaktovik	6.4	97%	Gaudreau *et al.* (2019)	Unknown	–
2018 Palu	7.5	3%	Socquet *et al.* (2019)*	150–250 km	Silver *et al.* (1983)
2019 Ridgecrest	6.4	30%	Xu *et al.* (2020)*	<20 m	Gold *et al.* (2021)
2019 Ridgecrest	7.1	29%	Xu *et al.* (2020)*	<100 m	Gold *et al.* (2021)
2020 Elazığ	6.8	85%	Pousse-Beltran *et al.* (2020)	9–26 km	Duman and Emre (2013)
2020 Stanley†	6.5	97%	Yang *et al.* (2021)	Unknown	–
2020 MCR	6.5	91%	This study	~600–700 m	This study
2020 Petrinja	6.4	84%	Xiong *et al.* (2022)	~560 m	Baize *et al.* (2022)
2021 Maduo	7.4	30%	Jin and Fialko (2021)	~2.5–5 km	Li Tao and Jinrui Liu, personal comm.
2022 Menyuan	6.6	54%	Yang *et al.* (2022)	95 ± 15 km	Gaudemer *et al.* (1995)

For each InSAR model, the SSD is equal to one minus the normalized slip of the surficial row of model subfault patches (the shallowest data point of the profile in Fig. 13) expressed as a percentage (e.g., Fialko *et al.*, 2005). Abbreviations: EMC, El Mayor-Cucapah; MCR, Monte Cristo range.
*Slip models that also incorporate near-field displacement fields from optical image correlation or differential lidar.
†InSAR model slip in the 2002 Nenana Mountain and the 2020 Stanley earthquakes peaks at 14 and 12.5 km depth, respectively (Wright *et al.*, 2003; Yang *et al.*, 2021).

only 600–700 m of cumulative offset. However, comparisons with InSAR slip models of 27 other continental, strike-slip earthquakes suggest that the pronounced SSD of the MCRE is controlled more by its moderate magnitude than by the structural immaturity of its host faults.

DATA AND RESOURCES

The supplemental material for this article includes Figures S1–S10, Tables S1–S3, and Data files S1–S3 (uploaded separately) showing the full results and supporting material of the Interferometric Synthetic Aperture Radar and Global Navigation Satellite System (InSAR–GNSS) inversion and forward models, and the seismological modeling. All data used in this study are freely available through the following platforms. SAR and multispectral images from Sentinel-1 and -2 satellites were accessed from the Alaska Satellite Facility (https://search.asf.alaska.edu, last accessed September 2020) and the Copernicus Open Access Hub (https://scihub.copernicus.eu, last accessed May 2022). We used the 3 arc-sec Shuttle Radar Topography Mission digital elevation model (DEM) obtained from OpenTopography (https://opentopography.org, last accessed May 2020) and the 1/3 arc-sec U.S. Geological Survey (USGS) 3D Elevation Program (3DEP) DEM (https://apps.nationalmap.gov/downloader, last accessed May 2022). Earthquake arrival times were collected from the International Seismological Centre (ISC) bulletin (DOI: 10.31905/D808B830) and the Advanced National Seismic System (ANSS) Comprehensive Earthquake Catalog (ComCat) system (DOI: 10.5066/P95R8K8G). Regional waveform data were obtained from Incorporated Research Institutions for Seismology (IRIS; http://ds.iris.edu/ds/nodes/dmc/data, last accessed December 2020) and the Nevada Seismological Laboratory, University of Nevada, Reno (UNR; http://www.seismo.unr.edu, last accessed December 2020). The GNSS coseismic offsets (19 June 2020 dataset) were obtained from Nevada Geodetic Laboratory (NGL; http://geodesy.unr.edu/news_items/20200619/nn00725272_24hr_19-Jun-2020.txt, last accessed November 2020). Uncrewed aerial system (UAS) survey data are in preparation for public release on OpenTopography by Pierce *et al.* Figures were plotted using the Generic Mapping Tools version 6 (Wessel *et al.*, 2019). Fault lines in figures were acquired from the USGS Quaternary fault and fold database (https://www.usgs.gov/natural-hazards/earthquake-hazards/faults, last accessed July 2021). Historic earthquake epicenters in figures were obtained from the USGS National Earthquake Information Center (NEIC) (https://earthquake.usgs.gov/earthquakes/search, last accessed May 2022). Sentinel-2 false color maps were generated using the open-source QGIS software. The paleoseismic trench orthomosaic was produced in Agisoft Metashape (https://www.agisoft.com, last accessed December 2020).

DECLARATION OF COMPETING INTERESTS

The authors acknowledge that there are no conflicts of interest recorded.

ACKNOWLEDGMENTS

The authors are grateful to Harley Benz for kindly helping them with the regional moment tensor (RMT) solutions, and for his support and encouragement of this work, to Austin Elliott and two anonymous reviewers, and to associate editor Richard Briggs for suggestions that improved this article. This study is funded through grants from the Natural Sciences and Engineering Research Council of Canada (NSERC), the Canada Foundation for Innovation (CFI), and the BC Knowledge Development Fund (BCKDF), as well as a University of Victoria Graduate Award, a James A. & Laurette Agnew Memorial Award, and an Anand-UVic Fund Graduate Scholarship to Israporn Sethanant, a Tier 2 Canada Research Chair to Edwin Nissen, and a Leverhulme Trust project "EROICA" to Ian Pierce.

REFERENCES

Aben, F. M., M. L. Doan, T. M. Mitchell, R. Toussaint, T. Reuschlé, M. Fondriest, J. P. Gratier, and F. Renard (2016). Dynamic fracturing by successive coseismic loadings leads to pulverization in active fault zones, *J. Geophys. Res.* **121,** no. 4, 2338–2360.

Aderhold, K., and R. E. Abercrombie (2015). Seismic rupture on an oceanic-continental plate boundary: Strike-slip earthquakes along the Queen Charlotte-Fairweather fault, *Bull. Seismol. Soc. Am.* **105,** no. 2B, 1129–1142.

Amoruso, A., L. Crescentini, and C. Fidani (2004). Effects of crustal layering on source parameter inversion from coseismic geodetic data, *Geophys. J. Int.* **159,** no. 1, 353–364.

Baize, S., S. Amoroso, N. Belić, L. Benedetti, P. Boncio, M. Budić, F. R. Cinti, M. Henriquet, P. Jamšek Rupnik, B. Kordić, *et al.* (2022). Environmental effects and seismogenic source characterization of the December 2020 earthquake sequence near Petrinja, Croatia, *Geophys. J. Int.* **230,** no. 2, 1394–1418.

Barbot, S., Y. Fialko, and D. Sandwell (2008). Effect of a compliant fault zone on the inferred earthquake slip distribution, *J. Geophys. Res.* **113,** no. B6, doi: 10.1029/2007JB005256.

Barnhart, W. D., G. P. Hayes, and R. D. Gold (2019). The July 2019 Ridgecrest, California, earthquake sequence: Kinematics of slip and stressing in cross-fault ruptures, *Geophys. Res. Lett.* **46,** no. 21, 11,859–11,867.

Bennett, R. A., B. P. Wernicke, N. A. Niemi, A. M. Friedrich, and J. L. Davis (2003). Contemporary strain rates in the northern Basin and Range province from GPS data, *Tectonics* **22,** no. 2, doi: 10.1029/2001TC001355.

Benz, H. M. (2021). Global catalog of calibrated earthquake locations, *U.S. Geol. Surv. Data Release*, doi: 10.1785/0220220217.

Berberian, M., J. A. Jackson, E. Fielding, B. E. Parsons, K. Priestley, M. Qorashi, M. Talebian, R. Walker, T. J. Wright, and C. Baker (2001). The 1998 March 14 Fandoqa earthquake (M_w 6.6) in Kerman province, southeast Iran: Re-rupture of the 1981 Sirch earthquake fault, triggering of slip on adjacent thrusts and the active tectonics of the Gowk fault zone, *Geophys. J. Int.* **146,** no. 2, 371–398.

Bergman, E. A., and S. C. Solomon (1990). Earthquake swarms on the Mid-Atlantic ridge: Products of magmatism or extensional tectonics? *J. Geophys. Res.* **95,** no. B4, 4943–4965.

Berryman, K. R., U. A. Cochran, K. J. Clark, G. P. Biasi, R. M. Langridge, and P. Villamor (2012). Major earthquakes occur regularly on an isolated plate boundary fault, *Science* **336,** no. 6089, 1690–1693.

Blewitt, G., W. C. Hammond, and C. Kreemer (2018). Harnessing the GPS data explosion for interdisciplinary science, *Eos* **99,** 10.1029/2018EO104623.

Bormann, J. M., W. C. Hammond, C. Kreemer, and G. Blewitt (2016). Accommodation of missing shear strain in the central Walker Lane, western North America: Constraints from dense GPS measurements, *Earth Planet. Sci. Lett.* **440,** 169–177.

Bormann, J. M., E. A. Morton, K. D. Smith, G. M. Kent, W. S. Honjas, G. L. Plank, and M. C. Williams (2021). Nevada seismological laboratory rapid seismic monitoring deployment and data availability for the 2020 M_w 6.5 Monte Cristo Range, Nevada, earthquake sequence, *Seismol. Res. Lett.* **92,** no. 2A, 810–822.

Bro, R., and S. De Jong (1997). A fast non-negativity-constrained least squares algorithm, *J. Chemom.* **11,** no. 5, 393–401.

Brodsky, E. E., J. J. Gilchrist, A. Sagy, and C. Collettini (2011). Faults smooth gradually as a function of slip, *Earth Planet. Sci. Lett.* **302,** nos. 1/2, 185–193.

Brooks, B. A., S. E. Minson, C. L. Glennie, J. M. Nevitt, T. Dawson, R. Rubin, T. L. Ericksen, D. Lockner, K. Hudnut, V. Langenheim, *et al.* 2017)). Buried shallow fault slip from the South Napa earthquake revealed by near-field geodesy, *Sci. Adv.* **3,** no. 7, e1700525, doi: 10.1126/sciadv.1700525.

Çakir, Z., J.-B. de Chabalier, R. Armijo, B. Meyer, A. Barka, and G. Peltzer (2003). Coseismic and early post-seismic slip associated with the 1999 Izmit earthquake (Turkey), from SAR interferometry and tectonic field observations, *Geophys. J. Int.* **155,** no. 1, 93–110.

Callaghan, E., and V. P. Gianella (1935). The earthquake of January 30, 1934, at Excelsior Mountains, Nevada, *Bull. Seismol. Soc. Am.* **25,** no. 2, 161–168.

Childs, C., T. Manzocchi, J. J. Walsh, C. G. Bonson, A. Nicol, and M. P. J. Schöpfer (2009). A geometric model of fault zone and fault rock thickness variations, *J. Struct. Geol.* **31,** no. 2, 117–127.

Childs, C., J. Watterson, and J. J. Walsh (1995). Fault overlap zones within developing normal fault systems, *J. Geol. Soc.* **152,** no. 3, 535–549.

Chounet, A., M. Vallée, M. Causse, and F. Courboulex (2018). Global catalog of earthquake rupture velocities shows anticorrelation between stress drop and rupture velocity, *Tectonophysics* **733,** 148–158.

Choy, G. L., and S. H. Kirby (2004). Apparent stress, fault maturity and seismic hazard for normal-fault earthquakes at subduction zones, *Geophys. J. Int.* **159,** no. 3, 991–1012.

Cole, J., R. McCabe, T. Moriarty, J. A. Malicse, F. G. Delfin, H. Tebar, and H. P. Ferrer (1989). A preliminary Neogene paleomagnetic data set from Leyte and its relation to motion on the Philippine fault, *Tectonophysics* **168,** no. 1, 205–220.

Cui, Y., Z. Ma, Y. Aoki, J. Liu, D. Yue, J. Hu, C. Zhou, and Z. Li (2021). Refining slip distribution in moderate earthquakes using Sentinel-1 burst overlap interferometry: A case study over 2020 May 15 M_w 6.5 Monte Cristo Range earthquake, *Geophys. J. Int.* **229,** 472–486.

Dee, S., R. D. Koehler, A. J. Elliott, A. E. Hatem, A. Pickering, I. Pierce, G. G. Seitz, C. M. Collett, T. E. Dawson, C. De Masi, *et al.* (2021). Surface rupture map of the 2020 M 6.5 Monte Cristo Range earthquake, Esmeralda and Mineral counties, Nevada, *Technical Report 190*, University of Nevada, Reno, Nevada.

DeLano, K., J. Lee, R. Roper, and A. Calvert (2019). Dextral, normal, and sinistral faulting across the eastern California shear zone-Mina deflection transition, California-Nevada, USA, *Geosphere* **15,** no. 4, 1206–1239.

Dohrenwend, J. C. (1982). Surficial geologic map of the Walker Lake 1 degree × 2 degrees quadrangle, Nevada-California, *U.S. Geol. Surv. Technical Rept. Miscellaneous Field Studies Map MF-1382-C*, Denver, Colorado.

Dokka, R. K., and C. J. Travis (1990). Role of the eastern California shear zone in accommodating Pacific-North American plate motion, *Geophys. Res. Lett.* **17,** no. 9, 1323–1326.

Dolan, J. F., and B. D. Haravitch (2014). How well do surface slip measurements track slip at depth in large strike-slip earthquakes? The importance of fault structural maturity in controlling on-fault slip versus off-fault surface deformation, *Earth Planet. Sci. Lett.* **388,** 38–47.

Duman, T. Y., and O. Emre (2013). The East Anatolian fault: Geometry, segmentation and jog characteristics, *Geol. Soc. Lond. Spec. Publ.* **372,** no. 1, 495–529.

Eisbacher, G. H. (1976). Sedimentology of the Dezadeash flysch and its implications for strike-slip faulting along the Denali fault, Yukon Territory and Alaska, *Can. J. Earth Sci.* **13,** no. 11, 1495–1513.

Elliott, J. R., E. K. Nissen, P. C. England, J. A. Jackson, S. Lamb, Z. Li, M. Oehlers, and B. Parsons (2012). Slip in the 2010-2011 Canterbury earthquakes, New Zealand, *J. Geophys. Res.* **117,** no. B3, doi: 10.1029/2011JB008868.

Elliott, J. R., B. Parsons, J. A. Jackson, X. Shan, R. A. Sloan, and R. T. Walker (2011). Depth segmentation of the seismogenic continental crust: The 2008 and 2009 Qaidam earthquakes, *Geophys. Res. Lett.* **38,** no. 6, L06305, doi: 10.1029/2011GL046897.

Farr, T. G., and M. Kobrick (2000). Shuttle radar topography mission produces a wealth of data, *Eos Trans AGU* **81,** no. 48, 583–585.

Faulkner, D. R., T. M. Mitchell, E. Jensen, and J. Cembrano (2011). Scaling of fault damage zones with displacement and the implications for fault growth processes, *J. Geophys. Res.* **116,** no. B5, doi: 10.1029/2010JB007788.

Feng, L., A. V. Newman, G. T. Farmer, P. Psimoulis, and S. C. Stiros (2010). Energetic rupture, coseismic and post-seismic response of the 2008 M_W 6.4 Achaia-Elia earthquake in northwestern Peloponnese, Greece: An indicator of an immature transform fault zone, *Geophys. J. Int.* **183,** no. 1, 103–110.

Feng, W., Y. Tian, Y. Zhang, S. Samsonov, R. Almeida, and P. Liu (2017). A slip gap of the 2016 M_w 6.6 Muji, Xinjiang, China, earthquake inferred from Sentinel-1 TOPS interferometry, *Seismol. Res. Lett.* **88,** no. 4, 1054–1064.

Ferguson, H. G., S. W. Muller, and S. H. Cathcart (1953). Geology of the Coaldale quadrangle, Nevada, *U.S. Geol. Surv. Technical Rept. Geologic Quadrangle Map GQ-23*, Denver, Colorado, doi: 10.3133/gq23.

Ferguson, H. G., S. W. Muller, and S. H. Cathcart (1954). Geology of the Mina quadrangle, Nevada, *U.S. Geol. Surv. Technical Rept. Geologic Quadrangle Map GQ-45*, Denver, Colorado.

Fialko, Y., D. Sandwell, M. Simons, and P. Rosen (2005). Three-dimensional deformation caused by the Bam, Iran, earthquake and the origin of shallow slip deficit, *Nature* **435,** no. 7040, 295–299.

Fielding, E. J., P. R. Lundgren, R. Bürgmann, and G. J. Funning (2009). Shallow fault-zone dilatancy recovery after the 2003 Bam earthquake in Iran, *Nature* **458,** no. 7234, 64–68.

Finzi, Y., E. H. Hearn, Y. Ben-Zion, and V. Lyakhovsky (2009). Structural properties and deformation patterns of evolving strike-slip faults: Numerical simulations incorporating damage rheology, *Pure Appl. Geophys.* **166,** nos. 10/11, 1537–1573.

Fletcher, J. M., O. J. Teran, T. K. Rockwell, M. E. Oskin, K. W. Hudnut, K. J. Mueller, R. M. Spelz, S. O. Akciz, E. Masana, G. Faneros, *et al.* (2014). Assembly of a large earthquake from a complex fault system: Surface rupture kinematics of the 4 April 2010 El Mayor-Cucapah (Mexico) M_w 7.2 earthquake, *Geosphere* **10,** no. 4, 797–827.

Floyd, M. A., R. J. Walters, J. R. Elliott, G. J. Funning, J. L. Svarc, J. R. Murray, A. J. Hooper, Y. Larsen, P. Marinkovic, R. Bürgmann, *et al.* (2016). Spatial variations in fault friction related to lithology from rupture and afterslip of the 2014 South Napa, California, earthquake, *Geophys. Res. Lett.* **43,** no. 13, 6808–6816.

Frost, E., J. Dolan, C. Sammis, B. Hacker, J. Cole, and L. Ratschbacher (2009). Progressive strain localization in a major strike-slip fault exhumed from midseismogenic depths: Structural observations from the Salzach-Ennstal-Mariazell-Puchberg fault system, Austria, *J. Geophys. Res.* **114,** no. B4, doi: 10.1029/2008JB005763.

Fu, B., and Y. Awata (2007). Displacement and timing of left-lateral faulting in the Kunlun fault zone, northern Tibet, inferred from geologic and geomorphic features, *J. Asian Earth Sci.* **29,** nos. 2/3, 253–265.

Funning, G. J., B. Parsons, and T. J. Wright (2007). Fault slip in the 1997 Manyi, Tibet earthquake from linear elastic modelling of InSAR displacements, *Geophys. J. Int.* **169,** no. 3, 988–1008.

Funning, G. J., B. Parsons, T. J. Wright, J. A. Jackson, and E. J. Fielding (2005). Surface displacements and source parameters of the 2003 Bam (Iran) earthquake from Envisat advanced synthetic aperture radar imagery, *J. Geophys. Res.* **110,** no. B9, doi: 10.1029/2004JB003338.

Gaudemer, Y., P. Tapponnier, B. Meyer, G. Peltzer, G. Shunmin, C. Zhitai, D. Huagung, and I. Cifuentes (1995). Partitioning of crustal slip between linked, active faults in the eastern Qilian Shan, and evidence for a major seismic gap, the 'Tianzhu gap', on the western Haiyuan Fault, Gansu (China), *Geophys. J. Int.* **120,** no. 3, 599–645.

Gaudreau, É., E. K. Nissen, E. A. Bergman, H. M. Benz, F. Tan, and E. Karasözen (2019). The August 2018 Kaktovik earthquakes: Active tectonics in northeastern Alaska revealed with InSAR and seismology, *Geophys. Res. Lett.* **46,** no. 24, 14,412–14,420.

Gold, R. D., C. B. DuRoss, and W. D. Barnhart (2021). Coseismic surface displacement in the 2019 Ridgecrest earthquakes: Comparison of field measurements and optical image correlation results, *Geochem. Geophys. Geosys.* **22,** no. 3, e09326, doi: 10.1029/2020GC009326.

Goldstein, R. M., and C. L. Werner (1998). Radar interferogram filtering for geophysical applications, *Geophys. Res. Lett.* **25,** no. 21, 4035–4038.

Gomberg, J. (1996). Stress/strain changes and triggered seismicity following the M_w 7.3 Landers, California earthquake, *J. Geophys. Res.* **101,** no. B1, 751–764.

Grondin, D. P., M. Petronis, J. Lindline, and B. P. Romero (2016). Vertical axis clockwise rotation of fault blocks in the eastern Mono basin, California and Nevada, *Geological Society of America Abstracts with Programs*, doi: 10.1130/ABS/2016AM-286303.

Hamling, I. J., S. Hreinsdóttir, K. Clark, J. Elliott, C. Liang, E. Fielding, N. Litchfield, P. Villamor, L. Wallace, T. J. Wright, *et al.* (2017). Complex multifault rupture during the 2016 M_w 7.8 Kaikōura earthquake, New Zealand, *Science* **356,** no. 6334, doi: 10.1126/science.aam7194.

Hammond, W. C., G. Blewitt, C. Kreemer, R. D. Koehler, and S. Dee (2021). Geodetic observation of seismic cycles before, during, and after the 2020 Monte Cristo Range, Nevada earthquake, *Seismol. Res. Lett.* **92,** no. 2A, 647–662.

Hatem, A. E., M. L. Cooke, and K. Toeneboehn (2017). Strain localization and evolving kinematic efficiency of initiating strike-slip faults within wet kaolin experiments, *J. Struct. Geol.* **101,** 96–108.

Hearn, E. H., and R. Bürgmann (2005). The effect of elastic layering on inversions of GPS Data for coseismic slip and resulting stress changes: Strike-slip earthquakes, *Bull. Seismol. Soc. Am.* **95,** no. 5, 1637–1653.

Hecker, S., T. E. Dawson, and D. P. Schwartz (2010). Normal-faulting slip maxima and stress-drop variability: A geological perspective, *Bull. Seismol. Soc. Am.* **100,** no. 6, 3130–3147.

Herrmann, R. B., H. Benz, and C. J. Ammon (2011). Monitoring the earthquake source process in North America, *Bull. Seismol. Soc. Am.* **101,** no. 6, 2609–2625.

Hicks, S. P., and A. Rietbrock (2015). Seismic slip on an upper-plate normal fault during a large subduction megathrust rupture, *Nat. Geosci.* **8,** no. 12, 955–960.

Hodgkinson, K. M., R. S. Stein, and G. C. P. King (1996). The 1954 Rainbow Mountain-Fairview Peak-Dixie Valley earthquakes: A triggered normal faulting sequence, *J. Geophys. Res.* **101,** no. B11, 25,459–25,471.

Huang, M. H., E. J. Fielding, H. Dickinson, J. Sun, J. A. Gonzalez-Ortega, A. M. Freed, and R. Bürgmann (2017). Fault geometry inversion and slip distribution of the 2010 M_w 7.2 El Mayor-Cucapah earthquake from geodetic data, *J. Geophys. Res.* **122,** no. 1, 607–621.

Huang, M.-H., H. Tung, E. J. Fielding, H.-H. Huang, C. Liang, C. Huang, and J.-C. Hu (2016). Multiple fault slip triggered above the 2016 M_w 6.4 MeiNong earthquake in Taiwan, *Geophys. Res. Lett.* **43,** no. 14, 7459–7467.

Hudnut, K. W., L. Seeber, and J. Pacheco (1989). Cross-fault triggering in the November 1987 Superstition Hills earthquake sequence, southern California, *Geophys. Res. Lett.* **16,** no. 2, 199–202.

Hull, J. (1988). Thickness-displacement relationships for deformation zones, *J. Struct. Geol.* **10,** no. 4, 431–435.

Hutchison, A. A., M. Böse, and I. Manighetti (2020). Improving early estimates of large earthquake's final fault lengths and magnitudes leveraging source fault structural maturity information, *Geophys. Res. Lett.* **47,** no. 14, doi: 10.1029/2020GL087539.

Jachens, R. C. (2002). Relationship of the 1999 Hector Mine and 1992 Landers fault ruptures to offsets on Neogene faults and distribution of late Cenozoic basins in the eastern California shear zone, *Bull. Seismol. Soc. Am.* **92,** no. 4, 1592–1605.

Jackson, J., M. Bouchon, E. Fielding, G. Funning, M. Ghorashi, D. Hatzfeld, H. Nazari, B. Parsons, K. Priestley, M. Talebian, *et al.* (2006). Seismotectonic, rupture process, and earthquake-hazard aspects of the 2003 December 26 Bam, Iran, earthquake, *Geophys. J. Int.* **166,** no. 3, 1270–1292.

Jin, Z., and Y. Fialko (2021). Coseismic and early postseismic deformation due to the 2021 M7.4 Maduo (China) earthquake, *Geophys. Res. Lett.* **48,** no. 21, doi: 10.1029/2021GL095213.

Johanson, I. A., E. J. Fielding, F. Rolandone, and R. Bürgmann (2006). Coseismic and postseismic slip of the 2004 Parkfield earthquake from space-geodetic data, *Bull. Seismol. Soc. Am.* **96,** no. 4B, 269–282.

Jones, L. E., S. E. Hough, and D. V. Helmberger (1993). Rupture process of the June 28, 1992 Big Bear earthquake, *Geophys. Res. Lett.* **20,** no. 18, 1907–1910.

Jongens, R., D. J. A. Barrell, J. K. Campbell, and J. R. Pettinga (2012). Faulting and folding beneath the Canterbury Plains identified prior to the 2010 emergence of the Greendale fault, *N. Z. J. Geol. Geophys.* **55,** no. 3, 169–176.

Jónsson, S., H. Zebker, P. Segall, and F. Amelung (2002). Fault slip distribution of the 1999 M_w 7.1 Hector Mine, California, earthquake, estimated from satellite radar and GPS measurements, *Bull. Seismol. Soc. Am.* **92,** no. 4, 1377–1389.

Kane, D. L., P. M. Shearer, B. P. Goertz-Allmann, and F. L. Vernon (2013). Rupture directivity of small earthquakes at Parkfield, *J. Geophys. Res.* **118,** no. 1, 212–221.

Kaneko, Y., and Y. Fialko (2011). Shallow slip deficit due to large strike-slip earthquakes in dynamic rupture simulations with elasto-plastic off-fault response, *Geophys. J. Int.* **186,** no. 3, 1389–1403.

Kaneko, Y., N. Lapusta, and J. P. Ampuero (2008). Spectral element modeling of spontaneous earthquake rupture on rate and state faults: Effect of velocity-strengthening friction at shallow depths, *J. Geophys. Res.* **113,** no. B9, doi: 10.1029/2007JB005553.

Karasözen, E., E. Nissen, E. A. Bergman, and A. Ghods (2019). Seismotectonics of the Zagros (Iran) from Orogen-Wide, calibrated earthquake relocations, *J. Geophys. Res.* **124,** no. 8, 9109–9129.

Kennett, B. L. N., E. R. Engdahl, and R. Buland (1995). Constraints on seismic velocities in the Earth from traveltimes, *Geophys. J. Int.* **122,** no. 1, 108–124.

Koehler, R. D., S. Dee, A. Elliott, A. Hatem, A. Pickering, I. Pierce, and G. Seitz (2021). Field response and surface-rupture characteristics of the 2020 M 6.5 Monte Cristo Range earthquake, central Walker Lane, Nevada, *Seismol. Res. Lett.* **92,** no. 2A, 823–839.

Lasserre, C., G. Peltzer, F. Crampé, Y. Klinger, J. van der Woerd, and P. Tapponnier (2005). Coseismic deformation of the 2001 $M_w =$ 7.8 Kokoxili earthquake in Tibet, measured by synthetic aperture radar interferometry, *J. Geophys. Res.* **110,** no. B12, doi: 10.1029/2004JB003500.

Lauer, B., R. Grandin, and Y. Klinger (2020). Fault geometry and slip distribution of the 2013 Mw 7.7 Balochistan earthquake from inversions of SAR and optical data, *J. Geophys. Res.* **125,** no. 7, doi: 10.1029/2019JB018380.

Lee, J., J. Garwood, D. F. Stockli, and J. Gosse (2009). Quaternary faulting in Queen Valley, California-Nevada: Implications for kinematics of fault-slip transfer in the eastern California shear zone-Walker Lane belt, *Geol. Soc. Am. Bull.* **121,** nos. 3/4, 599–614.

Lee, J., D. Stockli, J. Schroeder, C. Tincher, D. Bradley, L. Owen, J. Gosse, R. Finkel, and J. Garwood (2006). Fault slip transfer in the eastern California shear zone-Walker Lane belt, *Geological Society of America Penrose Conference Field Trip Guide (Kinematics and Geodynamics of Intraplate Dextral Shear in Eastern California and Western Nevada*, Mammoth Lakes, California, 21–26 April 2005.

Li, C., X. Wang, C. He, X. Wu, Z. Kong, and X. Li (2019). China national digital geological map (public version at 1:200 000 Scale) spatial database, *Geol. China* **46,** no. S1, 1–10.

Li, S., T. Tao, Y. Chen, P. He, F. Gao, X. Qu, and Y. Zhu (2021). Geodetic observation and modeling of the coseismic and postseismic deformations associated with the 2020 Mw 6.5 Monte Cristo earthquake, *Earth Space Sci.* **8,** no. 6, doi: 10.1029/2021EA001696.

Li, Y., R. Bürgmann, and B. Zhao (2020). Evidence of fault immaturity from shallow slip deficit and lack of postseismic deformation of the 2017 M_w 6.5 Jiuzhaigou earthquake, *Bull. Seismol. Soc. Am.* **110,** no. 1, 154–165.

Li, Z., J. R. Elliott, W. Feng, J. A. Jackson, B. E. Parsons, and R. J. Walters (2011). The 2010 M_W 6.8 Yushu (Qinghai, China) earthquake: Constraints provided by InSAR and body wave seismology, *J. Geophys. Res.* **116,** no. B10, doi: 10.1029/2011JB008358.

Lindsey, E. O., V. J. Sahakian, Y. Fialko, Y. Bock, S. Barbot, and T. K. Rockwell (2014). Interseismic strain localization in the San Jacinto fault zone, *Pure Appl. Geophys.* **171,** no. 11, 2937–2954.

Liu, C., T. Lay, F. F. Pollitz, J. Xu, and X. Xiong (2021). Seismic and geodetic analysis of rupture characteristics of the 2020 M_w 6.5 Monte Cristo Range, Nevada, earthquake, *Bull. Seismol. Soc. Am.* **111,** no. 6, 3226–3236.

Locke, A., P. Billingsley, and E. B. Mayo (1940). Sierra Nevada tectonic pattern, *Geol. Soc. Am. Bull.* **51,** no. 4, 513–539.

Lozos, J. C. (2022). Dynamic rupture modeling of coseismic interactions on orthogonal strike-slip faults, *Geophys. Res. Lett.* **49,** no. 5, e2021GL097585, doi: 10.1029/2021GL097585.

Mackenzie, D., J. R. Elliott, E. Altunel, R. T. Walker, Y. C. Kurban, J. L. Schwenninger, and B. Parsons (2016). Seismotectonics and rupture process of the M_W 7.1 2011 Van reverse-faulting earthquake, eastern Turkey, and implications for hazard in regions of distributed shortening, *Geophys. J. Int.* **206,** no. 1, 501–524.

Manighetti, I., M. Campillo, S. Bouley, and F. Cotton (2007). Earthquake scaling, fault segmentation, and structural maturity, *Earth Planet. Sci. Lett.* **253,** nos. 3/4, 429–438.

Manighetti, I., A. Mercier, and L. De Barros (2021). Fault trace corrugation and segmentation as a measure of fault structural maturity, *Geophys. Res. Lett.* **48,** no. 20, doi: 10.1029/2021GL095372.

Marchandon, M., J. Hollingsworth, and M. Radiguet (2021). Origin of the shallow slip deficit on a strike slip fault: Influence of elastic structure, topography, data coverage, and noise, *Earth Planet. Sci. Lett.* **554,** doi: 10.1016/j.epsl.2020.116696.

Marchandon, M., M. Vergnolle, H. Sudhaus, and O. Cavalié (2018). Fault geometry and slip distribution at depth of the 1997 Mw 7.2 Zirkuh earthquake: Contribution of near-field displacement data, *J. Geophys. Res.* **123,** no. 2, 1904–1924.

Marone, C. (1998). Laboratory-derived friction laws and their application to seismic faulting, *Annu. Rev. Earth Planet. Sci.* **26,** 643–696.

Marone, C. J., C. H. Scholtz, and R. Bilham (1991). On the mechanics of earthquake afterslip, *J. Geophys. Res.* **96,** no. B5, 8441–8452.

Matsu'ura, M. (1977). Inversion of geodetic data. Part II. Optimal model of conjugate fault system for the 1927 Tango earthquake, *J. Phys. Earth* **25,** no. 3, 233–255.

Milliner, C. W. D., J. F. Dolan, J. Hollingsworth, S. Leprince, F. Ayoub, and C. G. Sammis (2015). Quantifying near-field and off-fault deformation patterns of the 1992 M_w 7.3 Landers earthquake, *Geochem. Geophys. Geosys.* **16,** no. 5, 1577–1598.

Nagorsen-Rinke, S., J. Lee, and A. Calvert (2013). Pliocene sinistral slip across the Adobe Hills, eastern California–western Nevada: Kinematics of fault slip transfer across the Mina deflection, *Geosphere* **9,** no. 1, 37–53.

Nissen, E., J. R. Elliott, R. A. Sloan, T. J. Craig, G. J. Funning, A. Hutko, B. E. Parsons, and T. J. Wright (2016). Limitations of rupture forecasting exposed by instantaneously triggered earthquake doublet, *Nat. Geosci.* **9,** no. 4, 330–336.

Okada, Y. (1985). Surface deformation due to shear and tensile faults in a half-space, *Bull. Seismol. Soc. Am.* **75,** no. 4, 1135–1154.

Oldow, J. S., J. W. Geissman, and D. F. Stockli (2008). Evolution and strain reorganization within Late Neogene structural Stepovers linking the central Walker Lane and northern eastern California shear zone, western Great Basin, *Int. Geol. Rev.* **50,** no. 3, 270–290.

Oldow, J. S., G. Kohler, and R. A. Donelick (1994). Late Cenozoic extensional transfer in the Walker Lane strike-slip belt, Nevada, *Geology* **22,** no. 7, 637–640.

Oskin, M. E., J. R. Arrowsmith, A. H. Corona, A. J. Elliott, J. M. Fletcher, E. J. Fielding, P. O. Gold, J. J. G. Garcia, K. W. Hudnut, J. Liu-Zeng, *et al.* (2012). Near-field deformation from the El Mayor-Cucapah earthquake revealed by differential LIDAR, *Science* **335,** no. 6069, doi: 10.1126/science.1213778.

Peacock, D. C. P., and D. J. Sanderson (1991). Displacements, segment linkage and relay ramps in normal fault zones, *J. Struct. Geol.* **13,** no. 6, 721–733.

Perrin, C., I. Manighetti, J. P. Ampuero, F. Cappa, and Y. Gaudemer (2016). Location of largest earthquake slip and fast rupture controlled by along-strike change in fault structural maturity due to fault growth, *J. Geophys. Res.* **121,** no. 5, 3666–3685.

Perrin, C., F. Waldhauser, and C. H. Scholz (2021). The shear deformation zone and the smoothing of faults with displacement, *J. Geophys. Res.* **126,** no. 5, doi: 10.1029/2020JB020447.

Petronis, M. S., J. W. Geissman, J. S. Oldow, and W. C. McIntosh (2009). Late Miocene to Pliocene vertical-axis rotation attending development of the Silver Peak–Lone Mountain displacement transfer zone, west-central Nevada, in *Late Cenozoic Structure and Evolution of the Great Basin-Sierra Nevada Transition*, J. S. Oldow and P. H. Cashman (Editors), Vol. 447, Geological Society of America, Denver, Colorado, 215–253, doi: 10.1130/2009.2447(12).

Pierce, I. K. D., S. G. Wesnousky, L. A. Owen, J. M. Bormann, X. Li, and M. Caffee (2021). Accommodation of plate motion in an incipient strike slip system: The central Walker Lane, *Tectonics* **40,** no. 2, doi: 10.1029/2019TC005612.

Pitarka, A., L. A. Dalguer, S. M. Day, P. G. Somerville, and K. Dan (2009). Numerical study of ground-motion differences between buried-rupturing and surface-rupturing earthquakes, *Bull. Seismol. Soc. Am.* **99,** no. 3, 1521–1537.

Pousse-Beltran, L., E. Nissen, E. A. Bergman, M. D. Cambaz, É. Gaudreau, E. Karasözen, and F. Tan (2020). The 2020 M_w 6.8 Elazığ (Turkey) earthquake reveals rupture behavior of the east Anatolian fault, *Geophys. Res. Lett.* **47,** no. 13, doi: 10.1029/2020GL088136.

Powers, P. M., and T. H. Jordan (2010). Distribution of seismicity across strike-slip faults in California, *J. Geophys. Res.* **115,** no. B5, doi: 10.1029/2008JB006234.

Press, W. H., S. A. Teukolsky, W. T. Vetterling, and B. P. Flannery (1992). Downhill simplex method in multidimensions, in *Numerical Recipes in C: The Art of Scientific Computing*, Second Edition, Cambridge University Press, New York.

Radiguet, M., F. Cotton, I. Manighetti, M. Campillo, and J. Douglas (2009). Dependency of near-field ground motions on the structural maturity of the ruptured faults, *Bull. Seismol. Soc. Am.* **99,** no. 4, 2572–2581.

Ragon, T., A. Sladen, and M. Simons (2018). Accounting for uncertain fault geometry in earthquake source inversions—I: Theory and simplified application, *Geophys. J. Int.* **214,** no. 2, 1174–1190.

Robertson, E. G. (1983). Relationship of fault displacement to gouge and breccia thickness, *Am. Inst. Mining Eng. Trans.* **274,** 1426–1432.

Rockwell, T. K., L. Scott, T. Dawson, R. Langridge, W. Lettis, and Y. Klinger (2002). Lateral offsets on surveyed cultural features resulting from the 1999 Izmit and Duzce earthquakes, Turkey, *Bull. Seismol. Soc. Am.* **92,** no. 1, 79–94.

Rood, D. H., D. W. Burbank, S. W. Herman, and S. Bogue (2011). Rates and timing of vertical-axis block rotations across the central Sierra Nevada-Walker Lane transition in the Bodie Hills, California/Nevada, *Tectonics* **30,** no. 5, TC5013, doi: 10.1029/2010TC002754.

Roten, D., K. B. Olsen, and S. M. Day (2017). Off-fault deformations and shallow slip deficit from dynamic rupture simulations with fault zone plasticity, *Geophys. Res. Lett.* **44,** no. 15, 7733–7742.

Ruhl, C. J., E. A. Morton, J. M. Bormann, R. Hatch-Ibarra, G. Ichinose, and K. D. Smith (2021). Complex fault geometry of the 2020 M_W 6.5 Monte Cristo Range, Nevada earthquake sequence, *Seismol. Res. Lett.* **92,** no. 3, 1876–1890.

Sadeghi Chorsi, T., J. Braunmiller, F. Deng, N. Mueller, S. Kerstetter, R. J. Stern, and T. H. Dixon (2021). The May 15, 2020 M 6.5 Monte Cristo Range, Nevada, earthquake: Eyes in the sky, boots on the ground, and a chance for students to learn, *Int. Geol. Rev.* **64,** no. 19, 2683–2702.

Savage, H. M., and E. E. Brodsky (2011). Collateral damage: Evolution with displacement of fracture distribution and secondary fault strands in fault damage zones,*J. Geophys. Res.* **116,** no. B3, doi: 10.1029/2010JB007665.

Scholz, C. H. (1987). Wear and gouge formation in brittle faulting, *Geology* **15,** no. 6, 493–495.

Schwartz, D. P., and K. J. Coppersmith (1984). Fault behavior and characteristic earthquakes: Examples from the Wasatch and San Andreas fault zones,*J. Geophys. Res.* **89,** no. B7, 5681–5698.

Scott, C., J. Champenois, Y. Klinger, E. Nissen, T. Maruyama, T. Chiba, and R. Arrowsmith (2019). The 2016 M7 Kumamoto, Japan, earthquake slip field derived from a joint inversion of differential Lidar topography, optical correlation, and InSAR surface displacements, *Geophys. Res. Lett.* **46,** no. 12, 6341–6351.

Scott, C. P., J. R. Arrowsmith, E. Nissen, L. Lajoie, T. Maruyama, and T. Chiba (2018). The M7 2016 Kumamoto, Japan, earthquake: 3-D Deformation along the fault and within the damage zone constrained from differential Lidar topography,*J. Geophys. Res.* **123,** no. 7, 6138–6155.

Şengör, A. M. C., O. Tüysüz, C. Imren, M. Sakinç, H. Eyidoğan, N. Görür, X. Le Pichon, and C. Rangin (2005). The North Anatolian fault: A new look, *Annu. Rev. Earth Planet. Sci.* **33,** 37–112.

Shipton, Z. K., and P. A. Cowie (2001). Damage zone and slip-surface evolution over μm to km scales in high-porosity Navajo sandstone, Utah, *J. Struct. Geol. J. Struct. Geol.* **23,** no. 12, 1825–1844.

Silver, E. A., R. McCaffrey, and R. B. Smith (1983). Collision, rotation, and the initiation of subduction in the evolution of Sulawesi, Indonesia, *J. Geophys. Res.* **88,** no. B11, 9407–9418.

Simons, M., Y. Fialko, and L. Rivera (2002). Coseismic deformation from the 1999 Mw 7.1 Hector Mine, California, earthquake as inferred from InSAR and GPS observations, *Bull. Seismol. Soc. Am.* **92,** no. 4, 1390–1402.

Socquet, A., J. Hollingsworth, E. Pathier, and M. Bouchon (2019). Evidence of supershear during the 2018 magnitude 7.5 Palu earthquake from space geodesy, *Nat. Geosci.* **12,** no. 3, 192–199.

Speed, R. C., and A. H. Cogbill (1979). Candelaria and other left-oblique slip faults of the Candelaria region, Nevada, *Geol. Soc. Am. Bull.* **90,** no. 2, 149–163.

Stewart, J. H., and W. G. Ernst (1988). Tectonics of the Walker Lane belt, western Great Basin: Mesozoic and Cenozoic deformation in a zone of shear, in *Metamorphism and crustal evolution of the Western United States*, W. G. Ernst (Editor), Rubey, Vol. 7, Prentice Hall, Englewood Cliffs, New Jersey, 683–713.

Stirling, M. W., S. G. Wesnousky, and K. Shimazaki (1996). Fault trace complexity, cumulative slip, and the shape of the magnitude-frequency distribution for strike-slip faults: A global survey, *Geophys. J. Int.* **124,** no. 3, 833–868.

Teran, O. J., J. M. Fletcher, M. E. Oskin, T. K. Rockwell, K. W. Hudnut, R. M. Spelz, S. O. Akciz, A. P. Hernandez-Flores, and A. E. Morelan (2015). Geologic and structural controls on rupture zone fabric: A field-based study of the 2010 Mw 7.2 El Mayor-Cucapah earthquake surface rupture, *Geosphere* **11,** no. 3, 899–920.

Thakur, P., and Y. Huang (2021). Influence of fault zone maturity on fully dynamic earthquake cycles, *Geophys. Res. Lett.* **48,** no. 17, doi: 10.1029/2021GL094679.

Thatcher, W., and D. P. Hill (1991). Fault orientations in extensional and conjugate strike-slip environments and their implications, *Geology* **19,** no. 11, 1116–1120.

Thomas, M. Y., J.-P. Avouac, J. Champenois, J.-C. Lee, and L.-C. Kuo (2014). Spatiotemporal evolution of seismic and aseismic slip on the Longitudinal Valley fault, Taiwan, *J. Geophys. Res.* **119,** no. 6, 5114–5139.

Tong, X., D. T. Sandwell, and Y. Fialko (2010). Coseismic slip model of the 2008 Wenchuan earthquake derived from joint inversion of Interferometric Synthetic Aperture Radar, GPS, and field data, *J. Geophys. Res.* **115,** no. B4, doi: 10.1029/2009JB006625.

Vallage, A., Y. Klinger, R. Grandin, H. S. Bhat, and M. Pierrot-Deseilligny (2015). Inelastic surface deformation during the 2013 Mw 7.7 Balochistan, Pakistan, earthquake, *Geology* **43,** no. 12, 1079–1082.

Walker, R. T., E. A. Bergman, J. R. Elliott, E. J. Fielding, A. R. Ghods, M. Ghoraishi, J. Jackson, H. Nazari, M. Nemati, B. Oveisi, *et al.* (2013). The 2010-2011 South Rigan (Baluchestan) earthquake sequence and its implications for distributed deformation and earthquake hazard in southeast Iran, *Geophys. J. Int.* **193,** no. 1, 349–374.

Walker, R. T., E. A. Bergman, W. Szeliga, and E. J. Fielding (2011). Insights into the 1968-1997 Dasht-e-Bayaz and Zirkuh earthquake sequences, eastern Iran, from calibrated relocations, InSAR and high-resolution satellite imagery, *Geophys. J. Int.* **187,** no. 3, 1577–1603.

Walsh, J. J., and J. Watterson (1988). Analysis of the relationship between displacements and dimensions of faults, *J. Struct. Geol.* **10,** no. 3, 239–247.

Wang, K., Y. Zhu, E. Nissen, and Z.-K. Shen (2021). On the relevance of geodetic deformation rates to earthquake potential, *Geophys. Res. Lett.* **48,** no. 11, doi: 10.1029/2021GL093231.

Wang, S., C. Fan, G. Wang, and E. Wang (2008). Late Cenozoic deformation along the northwestern continuation of the Xianshuihe fault system, eastern Tibetan plateau, *Geol. Soc. Am. Bull.* **120,** nos. 3/4, 312–327.

Wechsler, N., Y. Ben-Zion, and S. Christofferson (2010). Evolving geometrical heterogeneities of fault trace data, *Geophys. J. Int.* **182,** no. 2, 551–567.

Wegmüller, U., C. Werner, T. Strozzi, A. Wiesmann, O. Frey, and M. Santoro (2016). Sentinel-1 support in the gamma software, *Procedia Comput. Sci.* **100,** 1305–1312.

Wesnousky, S. G. (1988). Seismological and structural evolution of strike-slip faults, *Nature* **335,** no. 6188, 340–343.

Wesnousky, S. G. (2005). Active faulting in the Walker Lane, *Tectonics* **24,** no. 3, TC3009, doi: 10.1029/2004TC001645.

Wesnousky, S. G. (2006). Predicting the endpoints of earthquake ruptures, *Nature* **444,** no. 7117, 358–360.

Wessel, P., J. F. Luis, L. Uieda, R. Scharroo, F. Wobbe, W. H. F. Smith, and D. Tian (2019). The Generic Mapping Tools version 6, *Geochem. Geophys. Geosys.* **20**, no. 11, 5556–5564.

Wetterauer, R. H. (1977). The Mina deflection—A new interpretation based on the history of the Lower Jurassic Dunlap formation, western Nevada, *PhD Thesis*, Northwestern University, Evanston, Illinois.

Wright, T. J., Z. Lu, and C. Wicks (2003). Source model for the M_w 6.7, 23 October 2002, Nenana Mountain earthquake (Alaska) from InSAR, *Geophys. Res. Lett.* **30,** no. 18, doi: 10.1029/2003GL018014.

Wright, T. J., Z. Lu, and C. Wicks (2004). Constraining the slip distribution and fault geometry of the M_w 7.9, 3 November 2002, Denali fault earthquake with Interferometric Synthetic Aperture Radar and global positioning system data, *Bull. Seismol. Soc. Am.* **94,** no. 6B, S175–S189.

Wright, T. J., B. E. Parsons, J. A. Jackson, M. Haynes, E. J. Fielding, P. C. England, and P. J. Clarke (1999). Source parameters of the 1 October 1995 Dinar (Turkey) earthquake from SAR interferometry and seismic bodywave modeling, *Earth Planet. Sci. Lett.* **172,** nos. 1/2, 23–37.

Xiong, W., P. Yu, W. Chen, G. Liu, B. Zhao, Z. Nie, and X. Qiao (2022). The 2020 M_w 6.4 Petrinja earthquake: A dextral event with large coseismic slip highlights a complex fault system in northwestern Croatia, *Geophys. J. Int.* **228,** no. 3, 1935–1945.

Xu, X., D. T. Sandwell, L. A. Ward, C. W. D. Milliner, B. R. Smith-Konter, P. Fang, and Y. Bock (2020). Surface deformation associated with fractures near the 2019 Ridgecrest earthquake sequence, *Science* **370,** no. 6516, 605–608.

Xu, X., X. Tong, D. T. Sandwell, C. W. Milliner, J. F. Dolan, J. Hollingsworth, S. Leprince, and F. Ayoub (2016). Refining the shallow slip deficit, *Geophys. J. Int.* **204**, no. 3, 1843–1862.

Yang, H., and S. Yao (2021). Shallow destructive earthquakes, *Earthq. Sci.* **34,** no. 1, 15–24.

Yang, H., D. Wang, R. Guo, M. Xie, Y. Zang, Y. Wang, Q. Yao, C. Cheng, Y. An, and Y. Zhang (2022). Rapid report of the 8 January 2022 M_s 6.9 Menyuan earthquake, Qinghai, China, *Earthq. Res. Adv.* **2,** no. 1, doi: 10.1016/j.eqrea.2022.100113.

Yang, J., H. Zhu, T. Lay, Y. Niu, L. Ye, Z. Lu, B. Luo, H. Kanamori, J. Huang, and Z. Li (2021). Multifault opposing dip strike slip and normal fault rupture during the 2020 M_w 6.5 Stanley, Idaho earthquake, *Geophys. Res. Lett.* **48,** no. 10, doi: 10.1029/2021GL092510.

Yang, Y. H., M. C. Tsai, J. C. Hu, M. A. Aurelio, M. Hashimoto, J. A. Escudero, Z. Su, and Q. Chen (2018). Coseismic slip deficit of the 2017 Mw 6.5 Ormoc earthquake that occurred along a creeping segment and geothermal field of the Philippine fault, *Geophys. Res. Lett.* **45,** no. 6, 2659–2668.

Yao, S., and H. Yang (2022). Hypocentral dependent shallow slip distribution and rupture extents along a strike-slip fault, *Earth Planet. Sci. Lett.* **578,** doi: 10.1016/j.epsl.2021.117296.

Zhang, H., C. Thurber, and P. Bedrosian (2009). Joint inversion for Vp, Vs, and Vp/Vs at SAFOD, Parkfield, California, *Geochem. Geophys. Geosys.* **10,** no. 11, Q11002, doi: 10.1029/2009GC002709.

Zheng, A., X. Chen, and W. Xu (2020). Present-day deformation mechanism of the Northeastern mina deflection revealed by the 2020 M_w 6.5 Monte Cristo Range earthquake, *Geophys. Res. Lett.* **47**, no. 22, doi: 10.1029/2020GL090142.

Zinke, R., J. F. Dolan, R. Van Dissen, J. R. Grenader, E. J. Rhodes, C. P. McGuire, R. M. Langridge, A. Nicol, and A. E. Hatem (2015). Evolution and progressive geomorphic manifestation of surface faulting: A comparison of the Wairau and Awatere faults, South Island, New Zealand, *Geology* **43,** no. 11, 1019–1022.

Zinke, R., J. Hollingsworth, and J. F. Dolan (2014). Surface slip and off-fault deformation patterns in the 2013 M_W 7.7 Balochistan, Pakistan earthquake: Implications for controls on the distribution of near-surface coseismic slip, *Geochem. Geophys. Geosys.* **15,** no. 12, 5034–5050.

Manuscript received 11 August 2022